

THESIS FOR THE DEGREE OF DOCTOR OF PHILOSOPHY

In situ Studies of Platinum Catalyst Sintering

Pooya Tabib Zadeh Adibi



Department of Physics
CHALMERS UNIVERSITY OF TECHNOLOGY
Göteborg, Sweden 2016

In situ Studies of Platinum Catalyst Sintering

© Pooya Tabib Zadeh Adibi, 2016.

ISBN: 978-91-7597-334-0

Doktorsavhandlingar vid Chalmers tekniska högskola

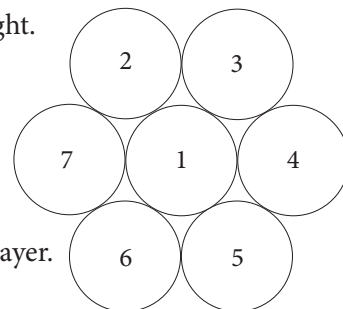
Ny serie Nr 4015

ISSN 0346-718X

Department of Physics
Chalmers University of Technology
SE-412 96 Göteborg, Sweden
Telephone + 46 (0)31-772 1000

Cover illustration

1. Two probes used in the thesis: high-energy electrons and visible light.
2. Bimodal size distribution of Pt nanoparticles.
3. Gold sensor particle covered with Pt-impregnated γ -alumina.
4. Pt particles on a nanocone and the surrounding flat area.
5. Pt sintering kinetic curves obtained by INPS.
6. Pt nanoparticles on a single gold sensor, separated by flat support layer.
7. TEM image of a Pt nanoparticle showing the atomic columns.



Printed at Chalmers Reproservice
Göteborg, Sweden 2016

Abstract

The damaging effect of pollutants from combustion engine exhaust on human health and environment is well recognized. Since the 70s, the three-way catalytic converter (TWC) has substantially improved the urban air quality by simultaneous conversion of CO, NO_x and unburned hydrocarbons to O₂, N₂ and H₂O. The active phase in the TWC is small precious metal particles (e.g. platinum, palladium, and rhodium) that are dispersed on high surface area oxide support such as γ -alumina. The TWC, however, has a limited durability due to catalyst deactivation where sintering is one major process at high temperatures. Presently, metal overloading is required for the TWC to meet legislations, and detailed understanding of sintering mechanisms and kinetics is crucial to design catalyst formulations with extended durability.

This thesis addresses fundamental issues connected to supported platinum sintering in oxidizing environments by two different approaches; (i) indirect nanoplasmonic sensing (INPS), as operando tool to probe the changes in an ensemble of Pt catalyst nanoparticles in real time, and (ii) transmission electron microscopy (TEM), by which Pt nanoparticles can be visualized after exposure to sintering conditions. By employing these tools, the sintering kinetics and evolution of Pt particle size distributions on alumina and silica supports are studied under oxidizing conditions.

In the first part of the thesis, the possibility to apply the INPS platform to study sintering on different flat supports in different gas environments is demonstrated. Time-resolved sintering kinetic data are deduced by correlating the INPS data with ex situ TEM analysis for Pt particles supported on silica and alumina in O₂ and NO₂ environment. The applicability of INPS is furthermore extended to monitor metal sintering in porous supports. This is achieved by successful deposition and metal impregnation of porous γ -alumina on the INPS sensor chip.

The second part of the thesis is dedicated to detailed TEM studies of Pt model catalyst sintering. Intermittent particle size distributions are analyzed as a function of time and temperature during oxygen-induced sintering of Pt on flat alumina and silica supports. Transient bimodal size distributions are clearly observed, and support heterogeneity is discussed as a possible mechanism. Moreover, controlled support heterogeneity was introduced by fabrication of an alumina support with arrays of nanocone structures. Significant differences in the evolution of Pt particle size and coverage on the cone and flat alumina surfaces are observed, with clear redispersion of Pt on the cones.

Keywords: platinum, catalyst deactivation, nanoparticle sintering, sintering kinetics, operando spectroscopy, indirect nanoplasmonic sensing, transmission electron microscopy

List of appended papers

The thesis is based on the following publications

Paper I

In Situ Plasmonic Sensing of Platinum Model Catalyst Sintering on Different Oxide Supports and in O₂ and NO₂ Atmospheres with Different Concentrations
Pooya Tabib Zadeh Adibi, Francesco Mazzotta, Tomasz J. Antosiewicz, Magnus Skoglundh, Henrik Grönbeck, and Christoph Langhammer
ACS Catalysis, 5, 426–432 (2015)

Paper II

Transient Bimodal Particle Size Distributions during Pt Sintering on Alumina and Silica
Pooya Tabib Zadeh Adibi, Vladimir P. Zhdanov, Christoph Langhammer, and Henrik Grönbeck
The Journal of Physical Chemistry C, 119, 989–996 (2015)

Paper III

Plasmonic Nanospectroscopy of Platinum Catalyst Nanoparticle Sintering in a Mesoporous Alumina Support
Pooya Tabib Zadeh Adibi, Torben Pingel, Eva Olsson, Henrik Grönbeck, and Christoph Langhammer
Submitted to *ACS Nano*

Paper IV

Pt Nanoparticle Sintering and Redispersion on a Heterogeneous Nanostructured Support
Pooya Tabib Zadeh Adibi, Torben Pingel, Eva Olsson, Henrik Grönbeck, and Christoph Langhammer
Submitted to *ACS Catalysis*

My contributions to the papers

Paper I

I performed all the experiments and the corresponding analysis except the INPS measurement of sintering in NO_2 . I wrote the first draft of the paper.

Paper II

I performed all the experiments and the corresponding analysis. I wrote the first draft of the paper.

Paper III

I performed all the experiments and the corresponding analysis except the STEM imaging. I wrote the first draft of the manuscript.

Paper IV

I fabricated the samples, performed the sintering experiments, a part of the TEM imaging, and analyzed the data. I wrote the first draft of the manuscript.

Contents

1	Introduction	1
	1.1. Heterogeneous catalysis	1
	1.2. Aim of the thesis	5
2	Catalyst Deactivation	7
	2.1. Deactivation mechanisms	7
	2.1.1. Models for particle sintering	11
	2.2. Factors controlling the sintering process	15
	2.2.1. Support effects	15
	2.2.2. Effect of temperature and gas environment	16
	2.3. Experimental techniques to study sintering	18
3	Sample Fabrication	23
	3.1. Hole-mask Collodial lithography	23
	3.2. Fabrication of model catalyst	26
	3.2.1. Support deposition	26
	3.2.2. Growth of Pt nanoparticles	27
	3.3. Synthesis of Pt catalyst in a porous alumina support	28
	3.4. TEM samples	31

4	Characterization Techniques	33
	4.1. Nanoplasmonic sensing	33
	4.1.1. Optical properties of metal nanoparticles	33
	4.1.2. Sensing principle	35
	4.1.3. Indirect nanoplasmonic sensing	37
	4.2. Transmission electron microscopy (TEM)	40
	4.3. Scanning electron microscopy (SEM)	42
	4.4. Ellipsometry	43
5	Summary of Results	45
6	Conclusions and Outlook	53
	Acknowledgments	57
	Bibliography	59

Introduction

1.1. Heterogeneous catalysis

Catalysis is a phenomenon in which a chemical reaction is accelerated by a substance called *catalyst*. Every one of us constantly experiences catalysis; from enzymes (biocatalyst) in our bodies that accelerate vital biological reactions like building up DNA, to breathing cleaner air provided by catalytic converters in vehicles. Catalysis can be divided into homogenous, heterogeneous and enzymatic. In homogeneous catalysis, the catalyst and the reactants are in the same phase (gas or liquid), while in heterogeneous catalysis, the phases of the reactants and the catalyst differ from each other. Enzymatic catalysis refers to processes in which enzymes catalyze biological reactions. The active catalytic phase may exist in several different forms including atoms, molecules, or particles¹.

In heterogeneous catalysis, reactions occur on the surface of a solid catalyst. Thus, in order to achieve high weight percentage of exposed atoms and to use the precious metal economically, nanometer-sized metal particles are often supported on mesoporous (containing pores with diameter of 2-50 nm)² oxides such as alumina or silica. In addition, smaller particles may exhibit an enhanced catalytic activity³. Gold is one example, which shows activity for oxidation reactions below a certain size^{4,5}. One of the reason for this size-dependence of gold is the higher concentration of step sites (that are known to be more catalytically active) for smaller particles⁶.

To elucidate the concept of heterogeneous catalytic reactions, catalytic CO oxidation is taken as an example (Figure 1.1). The catalytic cycle begins with adsorption of CO and O₂ on the surface of the catalyst where the O₂ molecule

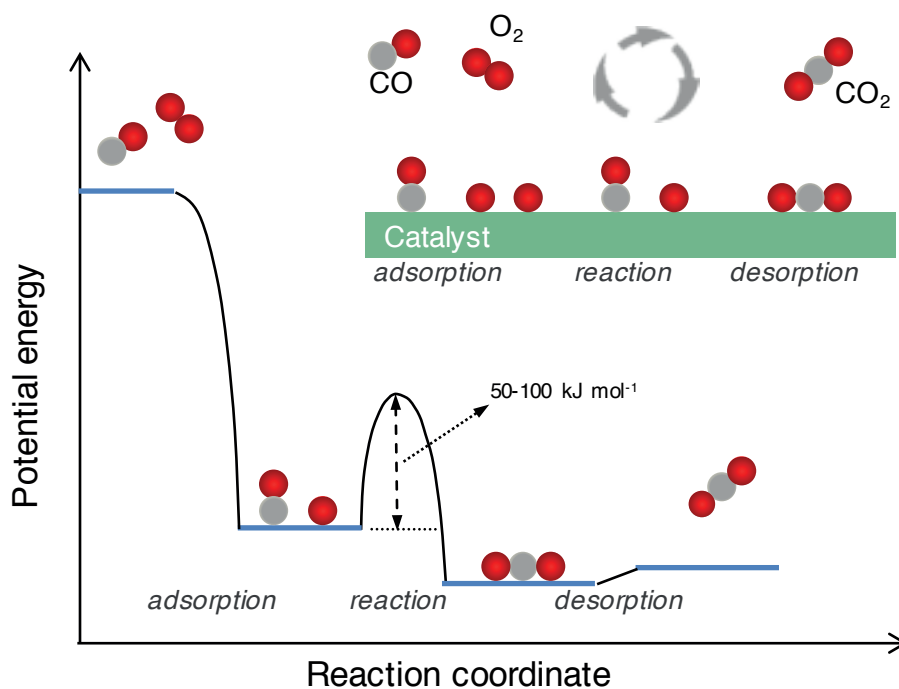


Figure 1.1. Potential energy diagram of CO oxidation by a catalyst. The inset shows the schematics of a catalytic cycle including adsorption of reactants on the catalyst surface, reaction and final desorption of product. Adapted from ref. [1].

dissociates into two oxygen atoms. The adsorbed O atom and CO molecule react on the catalyst surface to form stable CO_2 that is weakly bonded to the surface and desorbs, whereupon free site are formed for the next catalytic cycle¹. Figure 1.1 shows the schematic potential energy diagram and reaction cycle for catalytic oxidation of CO. The key point is that the activation energy for breaking the O-O bond in a gas phase reaction without catalyst is about 560 kJ/mol, whereas in the catalytic reaction, the O_2 molecule dissociates easily on the catalyst surface without sizable activation energy. The barrier for the catalyzed reaction instead originates from breaking the O-metal and CO-metal bonds. The described reaction path follows what generally is referred to as the Langmuir-Hinshelwood reaction path; the reactants absorb before reacting. One alternative path is the Eley-Rideal scheme, where one of the reactants reacts directly from the gas phase.

The reason why some metals are better catalysts for certain reactions lies on the catalyst-adsorbate interaction that influences the elementary steps in a catalytic cycle (i.e. adsorption, dissociation, reaction and desorption). The electronic structure of the metal surface and the adsorbate determines its reactivity for a specific reaction. For transition metals, the position of the d-band and the degree to which it is filled, as well as its relation to the electronic structure of adsorbates influence the reactivity¹.

For a given metal, electronic properties are influenced by the structure of the surface such as the crystallographic facet. For instance, it has been shown experimentally that Rh(111)⁷ dissociate NO more efficiently (i.e. lower activation energy) compared to Rh(100)⁸. Since nanoparticles of different shapes possess different types of facets and under-coordinated sites such as step edges, their shape becomes important in their reactivity towards certain reactions^{9,10}.

Generally, the interaction between the catalyst surface and the adsorbate should not be too strong or too weak. In case of weak interaction, the surface cannot dissociate the adsorbate molecule, while very strong adsorption does not allow the final desorption of the product from the surface. Thus, optimum interaction leads to high reactivity. This is referred to as Sabatier's principle.

In this thesis, we study supported Pt nanoparticles that are employed widely in automotive three-way catalytic converters (TWC). A brief overview of the TWC system and the issues of catalyst deactivation by sintering is provided below.

1.1.1. Three-way catalytic converter

Exhaust from combustion engines contains gases that are toxic for both humans¹² and the environment. The major pollutants are carbon monoxide (CO), nitrogen oxides (NO_x), unburned hydrocarbons, and particulate matter (e.g. soot). To control the emissions, legislative regulations have been established, starting with the Clean Air Act in the United States in 1970. Since then, similar regulations have been implemented worldwide. One of the first successful strategies to meet the regulations was the introduction of the three-way catalytic converter (TWC), which enables three main reactions, namely reduction of NO_x, and oxidation of CO and unburned hydrocarbons to N₂, H₂O, and CO₂. Figure 1.2 illustrates the typical structure of a TWC. It consists of a ceramic monolith that is coated with a 20-50 μm layer of high surface area oxide such as γ-alumina. The active phase of the TWC is precious metal particles such as platinum (Pt), palladium (Pd), and rhodium (Rh), which together with ceria and stabilizers, are dispersed on a mesoporous oxide. Generally, Pt and Pd exhibit good catalytic activity for oxidation of CO and hydrocarbons, while Rh is superior in NO_x reduction¹.

A catalytic converter should meet the standards with respect to the emissions and maintain activity over time. For example, the EU5/EU6 legislations require the TWC to meet the standards after 100,000 km or five years of usage¹³. One

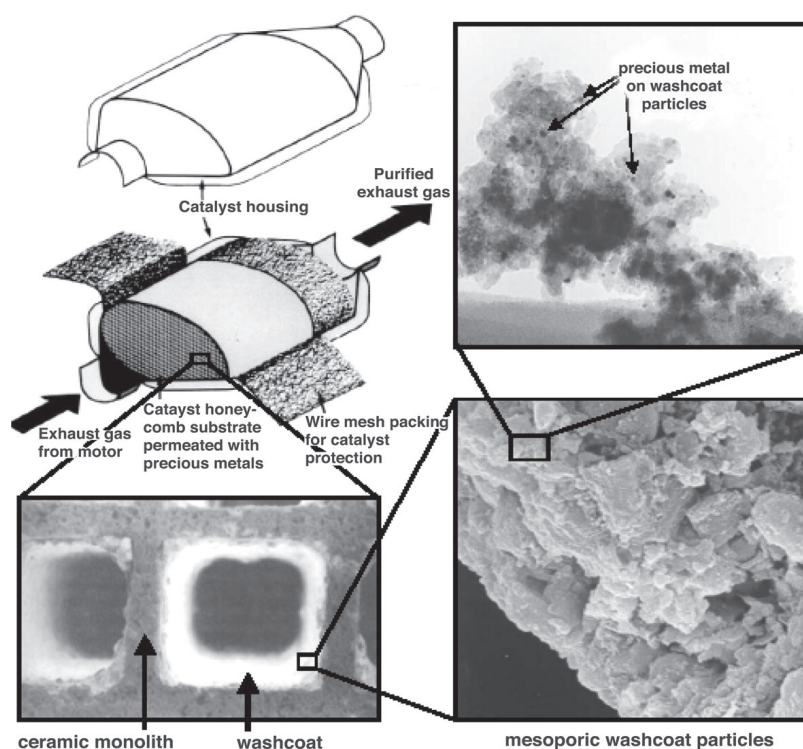


Figure 1.2. Illustration of the three-way catalytic converter (TWC). (Top left) Schematic of the TWC housing and the ceramic honeycomb. (Bottom left) SEM image of honeycomb channels coated with washcoat layer, (bottom right) SEM image of mesoporous washcoat, (top right) TEM image of catalyst nanoparticles supported on washcoat material. Reprinted with permission from ref. [11].

of the issues regarding the catalytic converters is that they are deactivated during operation¹⁴. Thermal damage, poisoning, and mechanical damage are the major causes.

One type of thermal damage is the coalescence of small particles into larger particles. This is an exothermic process that is driven by the large surface to volume ratio of small particles. Therefore, the active metal surface area on which the reactions occur is reduced over time, which leads to lower efficiency. Due to the deactivation, TWC manufacturers must design catalysts that initially perform well above the emission regulations. Excessive use of platinum group metals (Pt, Pd, and Rh) has considerable impact on the environment and industry. For example, mining of platinum group metals is associated with point-source pollution and mining waste at the extraction and refining sites¹⁵. Note that the automotive after-treatment is the largest market for platinum group metals. In 2012, automotive catalytic converters accounted for 56 % of the gross world demand for Pt, Pd, and Rh¹⁶.

Several strategies have been devised to stabilize the supported particles¹⁷. One solution is to slow down the sintering rate via alloying¹⁸ with a higher melting

point metal. For example, addition of Rh to Pt nanoparticles has been shown to be beneficial to suppress the sintering¹⁹. Another route for preparing more stable catalyst is encapsulation of nanoparticles with a thin, inert and porous oxide shell that acts as a shield to prevent/reduce the sintering. For instance, Somorjai and coworkers synthesized Pt particles coated with a mesoporous silica shell that shows high stability at 750 °C in air, while maintaining the same activity as bare Pt particles²⁰. Despite these attempts, there is still considerable room to find new ways to rationally design a more stable catalyst.

1.2. Aim of the thesis

A detailed complete understanding of sintering of catalyst systems in different conditions is missing, although the topic has been studied extensively during the past three decades. One reason is the complex nature of the process, in particular the metal-support interaction that varies over the surface of a heterogeneous mesoporous support. Therefore, we investigate the role of support material and in particular how the heterogeneity of the support can influence the sintering process. Another reason is related to the experimental tools that are typically used to monitor sintering. Despite the rapid progress in characterization tools (especially in situ measurements), there is still a limited number of suitable methods to follow sintering processes under realistic conditions. The thesis attempts to address these issues by developing an in situ method to study the sintering kinetics both on model and realistic catalyst systems.

The thesis is structured as follows. Chapter 2 introduces different deactivation mechanisms. Sintering of supported particles, that is the central topic of the studies, is explained in detail. Chapter 3 is dedicated to the sample fabrication. Chapter 4 presents the experimental techniques used in this work, with focus on *indirect nanoplasmonic sensing*. Chapter 5 summarizes the results, and finally, conclusions and outlook are provided in chapter 6.

Catalyst Deactivation

Inevitably, most catalysts deactivate during operation at high temperatures and in harsh gas environments. Deactivation is accompanied by reduced activity and/or lower selectivity to the desired products. The degree and time-scale of deactivation depends on the catalyst and the operating conditions. Iron catalysts in ammonia synthesis may last for 5 to 10 years, while cracking catalysts may be deactivated on the order of seconds²¹.

Catalyst deactivation leads to high additional costs due to replacement or regeneration of the catalyst. However, deactivation can to some extent be prevented, delayed or in some cases reversed²¹. Thus, there has been a considerable motivation to understand deactivation mechanisms thoroughly, in order to rationally design durable catalyst systems, as well as finding routes to slow down or even reverse the deactivation process. This chapter begins with discussion of five major deactivation mechanisms and examples relevant to the automotive catalytic converter²¹. Most attention will be paid to sintering of nanoparticles. Thereafter, a brief overview of factors that influence particle sintering is provided. Finally, different methods suitable for characterizing sintering of supported particles are introduced and compared.

2.1. Deactivation mechanisms

(a) Poisoning

Deactivation by poisoning is a mechanism where the number of active catalytic sites is decreased due to the chemisorption of atoms and molecules on the active metal or support surface. In some cases, the reactants or products strongly adsorb to the catalyst and act as poison (self-poisoning).

Chemisorbed species can influence the active sites in different ways: (1) by physically blocking the metal particles or the washcoat pores and consequently disabling reactant access to the metal catalyst, and (2) by inducing changes in the electronic and geometric structure of the surface, which affects the ability of a catalyst to adsorb or dissociate adsorbate molecules. For example, sulfur withdraws charge from the transition metals, which leads to a decrease in the density of states around the Fermi Level, and hence affects the catalytic activity²². It is found both theoretically and experimentally that the induced electronic changes have long-range effects^{23,24}. This means that a single sulfur atom chemisorbed on a metal catalyst site can poison the neighboring metal atoms as well.

The TWC can be deactivated by poisons such as phosphorous (from lubricating oil), lead, and sulfur. In automotive exhaust, sulfur originates from hydrocarbons such as thiophenes, which are oxidized to SO_2 during combustion and blocks the noble metal sites at temperatures below 300 °C^{1,25}. Above 300 °C, SO_2 can subsequently be oxidized to SO_3 , which is also a poison. Regeneration of SO_x poisoned catalysts is possible by exposing the catalyst to pure oxygen or hydrogen at high temperature. However, such treatments can often introduce problems such as reduction of oxide support (H_2) or oxidation of the metal catalyst (O_2)²². Often poisons can deactivate the catalyst irreversibly. As an example, misfueling by leaded fuel can poison the noble metals in the three-way catalyst, thus affecting the NO reduction activity irreversibly. The reason lies on the low surface energy of lead and its strong tendency to block the active sites¹.

(b) Gas–solid and solid-state reactions

Gas-solid reactions can deactivate the catalyst by reaction of the vapor phase with the catalyst to produce either an inactive phase or volatile compounds, which exit the reactor. On the other hand, solid-state reactions at operating conditions might lead to deactivation by transforming the active phase to a non-active phase. An example of these reactions in the automotive catalytic converter is the formation of the inactive phase of RuAl_2O_4 at high temperature (solid-state reaction), as well as the formation of volatile RuO_4 (gas-solid reaction). In general, this form of chemical deactivation can be suppressed by careful design of the operating conditions. Formation of volatile compounds can be prevented by operating at a temperature lower than the temperature for compound formation, or above the temperature for compound decomposition. A metal stabilizer can furthermore help to prevent/inhibit this process¹⁴.

(c) Fouling

Fouling refers to the deposition of species, such as carbon, onto the catalyst surface that leads to blockage of active sites and/or pores. In the three-way catalytic converter, carbon that can result from unburned hydrocarbons, may (1) partially or totally absorb (encapsulation) on active sites and thereby block access of reactants to the catalyst, and/or (2) block pores, which disables access of reactants to the particles inside these pores²¹. In order to prevent fouling, one can consider an operating condition at which carbon formation is minimized. If this is not possible, regeneration can be realized by combustion of deposited coke/carbon at low temperature.

(d) Mechanical deactivation

Mechanical failure is often observed in several forms including erosion and fracture²¹. Erosion of the catalyst due to high velocity motion of a fluid through it might lead to deactivation. While erosion is caused by mechanical stresses, fracture may have roots in mechanical, thermal or chemical stresses. For example, high temperature gradients and differences in thermal expansion coefficient between the washcoat and the monolith may lead to fracture of the washcoat and its separation from the monolith. Fracture can also be caused by chemical routes, such as generation of stress due to the formation of large amounts of carbon (according to mechanisms described above). Adding binders that have high fracture toughness (e.g. zirconia and titanates) can improve the adhesion between washcoat and substrate²⁶.

(e) Thermal degradation and sintering

Thermal processes result in deactivation of catalysts in several ways; (1) decrease in metal surface area due to ripening of catalyst nanoparticles, (2) loss of support surface area and pore collapse, and (3) solid-state reactions that chemically transform active phase to a non-catalytic phase (explained above). The first two phenomena are referred to as sintering, thermal aging or coarsening. Sintering processes occur at high temperature and depend strongly on temperature. In the TWC, the loss of support is often caused by phase transformation of γ -alumina to phases with lower surface area such as δ -alumina (at ca. 850 °C), θ -alumina (at ca. 1000 °C), or α -alumina (at ca. 1125 °C)¹. These irreversible conversions may result in the encapsulation of metal particles, rendering the catalyst inaccessible for the reactant. Adding specific amounts of stabilizers such as BaO, La₂O₃, SiO₂, and ZrO₂ can prevent support sintering. In the following, we focus on the sintering of supported

metal particles, which is the main theme of the thesis.

The driving force for nanoparticle sintering is reduction of total surface energy by forming larger particles with less under-coordinated atoms. Sintering is a complex physical and chemical process, which is affected by several parameters such as temperature, atmosphere, metal, support and promoter. In automotive catalytic converters, sintering of the precious metals has considerable environmental¹⁵ and economic impact. Detailed understanding of the mechanisms and kinetics of sintering is needed to formulate strategies that could limit the effect of this process. Generally, it is easier to limit or prevent sintering than to reverse it. Lowering the temperature (if possible) is the most direct solution. As a general rule of thumb, to minimize the sintering, the reaction temperature should be kept lower than 0.3-0.5 times the melting point of the metal catalyst²¹. To prevent the sintering of precious metals in three-way catalysts, ideally the exhaust temperature should be kept below ca. 800 °C¹. In recent years, this has been realized in automotive after-treatment by introducing more fuel-efficient vehicles that operate under lean conditions (lower fuel/air ratio) and consequently lower temperature (however, at low temperature ‘cold start’ issues arise²⁷). In some cases, chemical treatment with O₂ and/or Cl₂ (or other gases) can redisperse the sintered catalyst²⁸⁻³¹.

Two pathways for metal particle sintering are well accepted; The first mechanism is particle migration or Smoluchowski³² ripening, which involves the migration of entire particles over the support, followed by collision and coalescence. In fact, mobility of particle is realized by adatom diffusion on the surface of the nanoparticle (self-diffusion)³³. The second pathway is atomic migration or Ostwald ripening (named after Wilhelm Ostwald³⁴), in which atoms from smaller particles are transported to larger ones either via surface diffusion on the support or via the vapor phase. In the presence of adsorbate, Ostwald ripening can be mediated by mobile metal complexes/monomers (such as

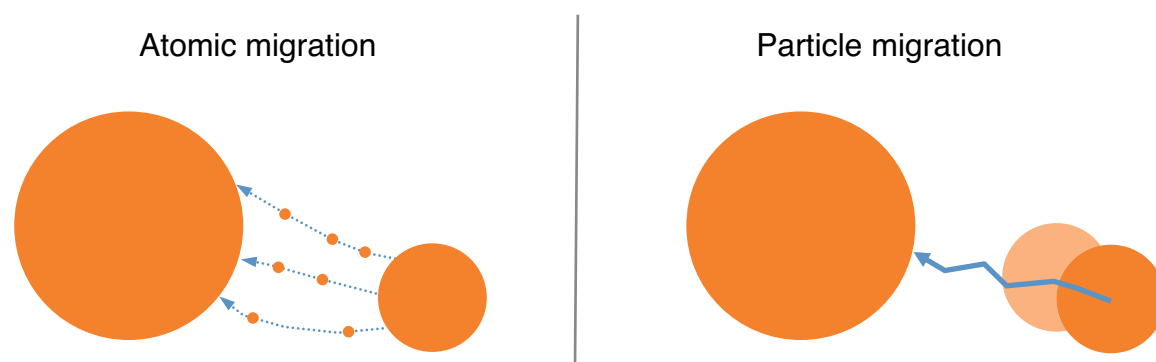


Figure 2.1. Simple illustration of particle sintering mechanisms: (left) atomic migration (Ostwald ripening), and (right) particle migration and coalescence.

oxides, carbonyls). Ostwald ripening can in principle have two different rate-limiting steps: detachment of the species from smaller particles (interface-controlled), and diffusion of the detached entities on the surface of the support or through the vapor phase (diffusion-controlled). Figure 2.1 shows a simple schematic of atomic migration and particle migration mechanisms.

Whether Ostwald ripening or particle migration occurs depends on the energetics of the catalyst system such as energy barriers for atom detachment, self-diffusion, atomic diffusion over the support, as well as adhesion energy between the metal atoms and the support³⁵. Ostwald ripening is more dominant over particle migration, if (a) the metal-support interaction is strong enough, so the support can anchor the monomers at their adsorption sites, and (b) the barrier for detachment of monomers is sufficiently low, so they can leave the particle³⁶. It is believed that smaller particles are more mobile and prone to particle migration, because the adatom diffusion rate over the particle strongly depends on its size³⁷.

It should be emphasized that due to the complexity of the supported catalyst systems (e.g. support heterogeneity) and size-dependence energetics³⁸, it is possible that both mechanisms occur at the same time, and their contribution changes over the course of the aging time³⁵.

Theoretical models describing Ostwald ripening and particle migration are briefly discussed in the following.

2.1.1. Models for particle sintering

During recent decades, several models for sintering and redispersion have been put forward. The models have different bases³⁹; thermodynamic models that are based on statistics of ensembles of particles, mechanistic models that deal with processes at the single particle level (e.g. Monte-Carlo simulations⁴⁰⁻⁴³), and empirical models such as the power law expressions that are explained below.

Empirical models were developed to allow better comparison with experimental results based on ensemble-averaged parameters such as dispersion (the ratio of active surface atoms to total metal atoms) or mean diameter. Two power law expressions (simple and general) have been proposed, which can be applied to both Ostwald ripening and particle migration mechanisms, and possibly predict the sintering mechanism. The first empirical model is the simple power law expression (SPLE)⁴⁴:

$$-\frac{d(D/D_0)}{dt} = k_s(D/D_0)^n \quad (2.1)$$

Where D is the dispersion, D_0 the initial dispersion, k_s the rate constant, and n is the sintering order. It has been suggested that the sintering order, n , can predict the sintering mechanism. Theoretical studies predict n in the range of 3 to 4 for Ostwald ripening^{33,42,45,46}, while n between 5 and 7 is proposed for particle migration^{33,44}. These predictions have been made by different types of kinetic models. For instance, Wynblatt and Gjostein⁴⁷ treated the growth and decay of individual particles via interparticle atomic exchange, while Ruckenstein and Pulvermacher⁴⁴ developed a diffusion and coalescence model assuming that the diffusion coefficient of a particle is size-dependent. However, experimental results show that the sintering order may vary from 3 to 15 and is a function of sintering time¹⁴. It should be noted that the theoretical studies have not taken into account the complexity of the support, which plays a key role in sintering processes. Furthermore, employing SPLE to fit the experimental kinetic data is debatable, as it assumes that dispersion converges to zero after sufficient time. In reality, however, asymptotic dispersion is observed after a long sintering time. By taking the observed asymptotic dispersion into account, the general power law expression (GPLe)^{48,49} can be applied to fit sintering kinetic data:

$$-\frac{d(D/D_0)}{dt} = k_s(D/D_0 - D_{eq}/D_0)^m \quad (2.2)$$

where D_{eq} is the dispersion at infinite time, and m is the sintering order that is found to be 1 or 2 by fitting to experimental kinetic data on technical catalysts. Using GPLe enables to quantify the correlation between the sintering rate and catalyst properties/sintering conditions⁴⁹. However, no prediction of sintering mechanism was suggested using equation 2.2.

The described empirical models do not consider the thermodynamical processes that are involved in particle sintering. Below, such models for both Ostwald ripening and particle migration are briefly discussed.

2.1.1.1. Ostwald ripening

The difference in chemical potential of particles determines the rate of atomic transport between them. The chemical potential of a particle, μ , with curvature radius of R can be expressed by the Gibbs-Thomson equation⁴⁷,

$$\mu = \mu_0 + 2\gamma\Omega/R \quad (2.3)$$

where μ_0 is the chemical potential of an infinitely large particle, γ is the particle surface energy, and Ω is the atomic volume. Small particles have larger chemical potential, hence, larger particles grow at the expense of smaller ones. Thus, one strategy to reduce the driving force for Ostwald ripening is to minimize the size variation of particles. This has been demonstrated experimentally by annealing two different samples, monomodal size-selected Pt clusters (Pt_{22} or Pt_{68}) and a bimodal distribution of size-selected clusters ($\text{Pt}_{22} + \text{Pt}_{68}$)⁵⁰. Almost no sintering was observed for a monomodal distribution, whereas the sample with bimodal distribution of clusters had undergone a notable ripening due to the gradients in the chemical potential of clusters with different size.

Based on the Gibbs-Thomson relation, Lifshitz and Slyozov⁵¹ and Wagner⁵² (LSW) developed a model that statistically describes the Ostwald ripening of spherical particles in a three-dimensional homogenous medium. The LSW model predicts an asymptotic particle size distribution (PSD) that is independent of the initial PSD and does not change with time after a transient period. The characteristic PSD has a tail toward the smaller particle side of the main peak (Figure 2.2 left). Later on, Chakraverty⁵³ adopted the LSW model for particles (spherical cap) on two-dimensional homogenous support and predicted similar asymptotic PSD shape. According to his model, particles cannot grow more than twice the average⁵³.

Wynblatt and Gjostein⁴⁷ modeled the growth and decay of individual particles (spherical cap on flat homogenous support), rather than employing a statistical description of an ensemble of particles. Their model establishes the growth rate for both interface-controlled and diffusion controlled ripening by considering the elementary steps for ripening (e.g., monomer detachments and diffusion).

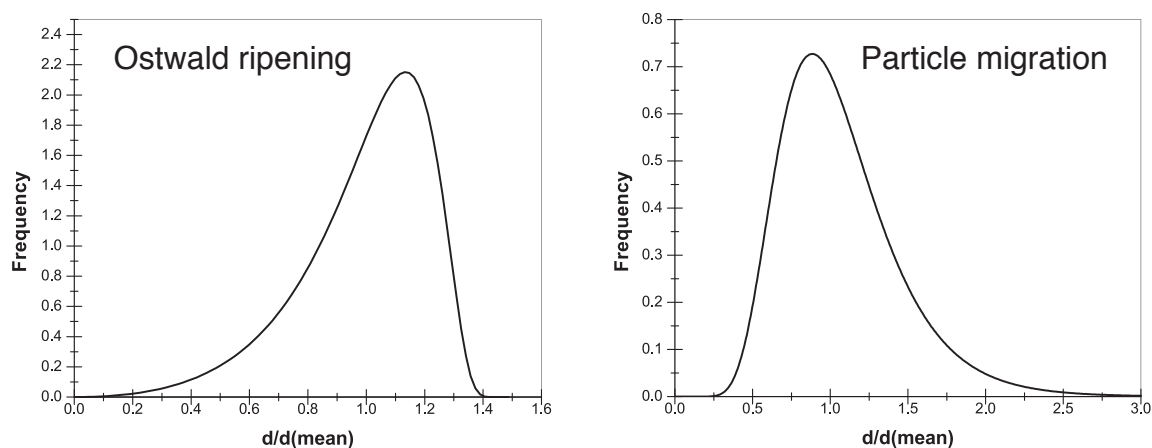


Figure 2.2. Theoretical predictions of particle size distribution of particles after sintering via (left) Ostwald ripening, and (right) particle migration. Reprinted with kind permission from⁶⁰.

The rate equation depends on parameters such as the temperature, the metal-support contact angle, metal surface energy, the diffusivity, and detachment activation energy. Campbell et al. further improved the ripening model for the interface-controlled regime by incorporating the size-dependent surface energy of the particles^{38,45}. More recently, atomistic models for Ostwald ripening and disintegration have been proposed with a focus on the role of adsorbates and the reaction conditions (e.g. pressure)^{54,55}.

2.1.1.2. Particle migration and coalescence

Provided they are given enough energy, atoms on the surface of a particle can move around. When the diffusion length is comparable to the particle diameter, this motion leads to displacement of the particle in a Brownian type motion. The displacement of a particle undergoing Brownian motion is,

$$X = 2\sqrt{D_p t} \quad (2.4)$$

where D_p is particle diffusion coefficient and t is time. Gruber⁵⁶ derived this parameter for a spherical bubble migrating in a three-dimensional solid, and later Willertz and Shewmon⁵⁷ found an expression for D_p by assuming faceted particles. Another model is the binary collision model^{44,58}, in which either migration or the coalescence can be the rate limiting step. It has been shown that the PSD for particles that have sintered by particle migration and coalescence can be fitted by a log-normal distribution function that has a tail toward the larger diameter side of the peak (Figure 2.2 right)⁵⁹.

According to Figure 2.2, one can imagine that comparing experimentally obtained PSDs after sintering with the theoretical predictions can be a route to deduce the sintering mechanism. Observation of Ostwald ripening of model catalysts such as Ge on Si⁶¹ and Ag/Ag(110)⁶² shows a PSD skewed to the right that is in agreement with the Ostwald ripening theory (LSW model). However, Datye et al. argued that none of the sintered industrial-style catalysts exhibit a PSD with a tail toward smaller particles, even for a system where Ostwald ripening is favored⁶³. Therefore, drawing conclusions on the sintering mechanism by evaluating the PSD alone is not definitive⁶³. Previously, Wanke questioned the use of PSDs for finding the mechanism, by arguing that the PSD of sintered particles strongly depends on the initial size distribution⁶⁴.

2.2. Factors controlling the sintering process

Recently, several attempts have been made to find the dominant particle sintering mechanism for different catalysts and conditions. The most conclusive way to find the sintering mechanism is to “see” the processes at the particle (or atomic) level using methods such as in situ TEM⁶⁵ or time-resolved STM^{62,66}. Such studies, despite detailed mechanistic view they make accessible, are often performed on model catalysts and/or in the low-pressure regime (see Figure 2.3). Another approach is to infer the mechanism from indirect measurements (either ex situ or in situ) by two routes: (1) particle size distribution analysis, and (2) fitting the experimental kinetic data (e.g. change of dispersion over the sintering time) to power-law expressions. The application and validity of these methods were discussed in the previous section.

Considerable effort has also been put into elucidating the role of several different parameters in sintering of metal particles. These factors include temperature, metal composition⁶⁷, nanoparticle geometry (size^{38,68}/shape⁶⁹) and distribution, interparticle distance⁷⁰⁻⁷², support, pretreatment⁷³, and environment (gas composition and pressure). To compare the results from different studies, one should consider the experimental details to avoid generalizing the effect of one parameter. We briefly survey the support effect and role of temperature and gas environment, which are relevant to this thesis.

2.2.1. Support effects

Support material plays an important role in sintering of particles by directly influencing processes such as detachment of adatoms and diffusion of monomers over the support. In general, comparing supports is a difficult task due to their chemical and morphological complexities, as well as inhomogeneity within porous supports. This might be one of the reasons for some contradictory results in the literature. For instance, compared with alumina, higher^{74,75}, comparable⁷⁶, and lower⁷⁷ degrees of Pt sintering have been reported on silica. Even for a simple case of sintering of Ag clusters on Ag single crystals, different sintering mechanisms have been observed, namely Ostwald ripening on Ag(111)^{78a} and particle migration on Ag(100)^{78b}.

Here, we divide the support effect into “structural” and “chemical” as follows. With respect to the structure, it has been shown that irregularities on the support, such as step edges, may trap the metal species and make them more stable⁷⁹. For example, vacuum annealing of Pt particles supported on TiO₂(110)⁸⁰ and TiO₂(771)⁸¹ results in higher population of particles along the step edges that

act as trapping sites. Moreover, local curvature of the support has an impact on the particle chemical potential and hence sintering behavior⁸². Specifically, it has been shown both theoretically and experimentally that particles tend to move from concave regions to convex (valley) regions to reduce their radius of curvature and thus chemical potential (see equation 2.3). Furthermore, when comparing the results from flat surfaces with realistic supports, one should note that particles on mesoporous supports are located in pore structures that may separate particles from each other, which may hinder the sintering. In addition, if ripening is mediated by transport of volatile metal oxides, redeposition of metal complexes within the pores of a mesoporous support is expected, whereas these monomers can be swept away in the case of flat support¹⁸.

Beyond the morphology, the chemical properties of a support also influence the coarsening of particles^{83,84}. The nature of the support material, impurities (e.g. promoters), surface hydroxyl⁸⁵⁻⁸⁷ and oxygen vacancies are among the factors that influence metal-support adhesion energy and consequently sintering. For example, the stabilizing effect of ceria (CeO_2), which is the oxygen storage component in TWCs, has been shown^{88,89}. In an oxidizing environment, formation of strong Pt-O-Ce bonds are proposed to act as anchors that suppress sintering via vapor phase and diffusion of species⁹⁰. The underlying thermodynamic reasons behind the stabilizing effect of ceria have been elucidated by Campbell et al.⁹¹. Calorimetric measurements show larger adhesion energy of Ag to $\text{CeO}_2(111)$ compared to an $\text{MgO}(100)$ surface. Moreover, a higher amount of oxygen vacancies in ceria (i.e. extent of ceria reduction) increases the metal-oxide adhesion, and thus more reduced ceria stabilizes the metal particles⁹¹.

2.2.2. Effect of temperature and gas environment

Particle sintering rates depend exponentially on the temperature as described by the Arrhenius expression^{14,49}. Both Ostwald ripening and particle migration involve steps that are affected by the temperature, namely self-diffusion and detachment of metal atoms (or metal complexes), and diffusion of these species over the support. For example, Fiedorow et al. reported redispersion of Pt/ Al_2O_3 in O_2 at temperatures below 600 °C, while at higher temperatures they observed sintering⁹².

Sintering and redispersion of particles are greatly influenced by the gas environment in the following ways: (a) Formation of metal complexes (e.g. Pt-O species in an oxidizing environment^{33,93,94}) influences particle stability

by reducing the complex detachment barrier (compared to metal adatom) and/or via desorption of volatile metal complexes. Previous experiments on model catalysts demonstrate enhanced self-diffusion of Pt by hydrogen⁹⁵ and Cu by sulfur⁹⁶, and more recently, CO-induced Pd/Fe₃O₄ sintering⁶⁶. (b) Gas-induced structural change of nanoparticles⁹⁷⁻¹⁰⁴ can, for instance, change the particle contact angle to the support and subsequently the radius of curvature that (according to eq. 2.3) alters the chemical potential and thus influences the sintering processes⁵⁴. In addition to the adsorbate-induced changes in the chemistry and morphology of nanoparticles, (c) support properties such as structure, chemical state, and defect density might be altered by gas adsorbates, which in turns influence the stability of the particles^{85,86}. Moreover, (d) the heat released by reactions on the catalyst can facilitate Ostwald ripening⁶⁸. For instance, Ostwald ripening of mass-selected gold nanoparticles has been observed in the mixture of CO and O₂ (exothermic CO oxidation), and not in CO alone⁶⁸.

Here, we briefly summarize oxygen-induced sintering that is relevant to this thesis. In an oxidizing environment and at high temperature PtO_x can form¹⁰⁵, however the role of these species with respect to the stability of Pt nanoparticles under different conditions is not clear¹⁰⁶. For the case of Pt/alumina catalysts in an oxidizing environment, some studies reported redispersion of Pt particles after aging at temperatures below 600 °C on both flat^{28,107-111} and mesoporous support^{67,76,92,112-115}, while others observed enhanced particle sintering (often) at higher temperatures on flat¹¹⁶ and high surface area support^{49,114,115,117}. It also has been shown that pretreatment of Pt/alumina in O₂ at temperatures between 400-500 °C has an stabilizing effect^{73,118-120}. One possible route for oxygen-induced particle redispersion is detachment of PtO_x species followed by migration to support defects where they get trapped. The surface defects act as nucleation sites to generate new particles. Thus, redispersion via this path requires defective support and low metal loading (or large interparticle distances)¹⁰⁹. On the other hand, oxygen-induced sintering has been explained by exchange of volatile PtO_x between the particles (Ostwald ripening through vapor phase), or detachment of PtO_x species (with lower detachment activation energy compared with Pt) over the support, followed by attachment to a neighboring particle^{33,116,118,121}. It is believed that monomer transport via the gas phase typically demands higher temperature¹⁸. We should also note that several parameters influence the redispersion and sintering processes at the same time. Ouyang et al.⁵⁴ theoretically showed that for a given metal and reactant, support material and reaction conditions (pressure and temperature) play a role in disintegration of metal complexes and possible sintering/redispersion.

2.3. Experimental techniques to study sintering

Two main approaches can be adopted to study sintering in heterogeneous catalysis³⁵. The first is to use model catalyst systems in ultra high vacuum (UHV) as demanded by traditional surface science tools. To study sintering, real catalysts can be experimentally modeled by depositing metal nanoparticles on flat support (single- or poly-crystalline)¹²². However, real catalysis occurs on complex material systems at high pressures (1 atm or higher), and experimental results from model catalysts in UHV are often quite different from realistic systems and conditions. This is known as the material and pressure gaps. Nevertheless, considerable efforts have been dedicated to bridge the material and pressure gap for traditional surface science tools¹²³⁻¹²⁶.

The second approach is the study of real catalysts (e.g. particles dispersed on a mesoporous support) at high pressure (atmospheric pressure or above) and temperature, which offers results comparable to industrial catalysis. In general, techniques capable of operating at high pressure often lack sufficient surface sensitivity for atom-by-atom characterization, while the surface science approach on model catalysts gives details at the nanoscale but with limited relevance to real catalysis.

It is also useful to categorize the experiments based on how the data are acquired after/during the course of aging. In “post mortem” or “ex situ” (Latin for off-site) measurements, one collects the data after the aging of the catalyst, while “in situ” (Latin for on-site) experiments monitor the status of the catalyst during the sintering. The in situ studies performed at conditions close to the operating conditions (e.g. high pressure and temperature) are called “in operando” or simply “operando”.

The degree of particle sintering can be measured by parameters such as particle size and distribution as well as dispersion. Several techniques relevant to investigate sintering are discussed below. Figure 2.3 illustrates the applicability of those tools regarding their typical applied pressure and catalyst type that can be investigated.

Transmission electron microscopy (TEM) is a direct way to estimate the particle size and distribution by imaging the projected area of the catalyst particles on both mesoporous and flat support¹²⁷. Besides the projection imaging, the major complication with TEM analysis is that small particles (< 1 nm) might be overlooked due to the low contrast, and it is hard to distinguish overlapping particles. Although TEM does not provide information on the 3D shape of

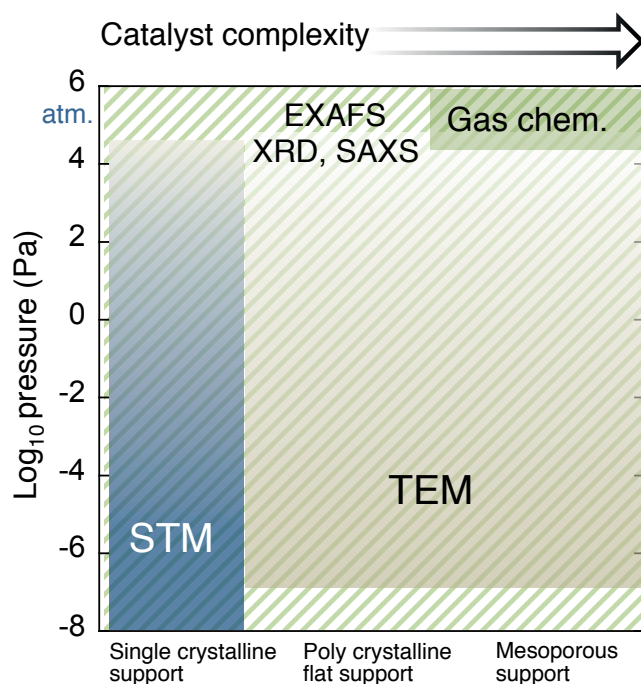


Figure 2.3. Applicability of different techniques to study particle sintering with respect to the applied pressure and the catalyst complexity.

the particles, there exist methods to gain such information by, for example, electron tomography^{128,129}, and combining scanning TEM (STEM) with other techniques such as extended X-ray absorption fine structure (EXAFS)^{130,131} or modeling^{132,133}. In addition, cross-sectional TEM imaging^{99,102,103,134} can be employed to visualize the nanoparticle/support contact (i.e. the wetting properties of particles on the support) that are important for sintering.

In recent years, environmental transmission electron microscopy (ETEM)^{135,136} has emerged as one of the most common in situ methods to follow sintering processes⁶⁵. However, most of those studies have been performed at much lower pressure compared to operating conditions^{116,121,137–144}. An example of an in situ TEM study is shown in Figure 2.4 (top row), where the evolution of Pt particles supported on alumina in 10 mbar technical air at 650 °C confirms Ostwald ripening as the main sintering mechanism. It has also been shown that by using a windowed gas cell¹⁴⁵ (instead of differential pumping approach), environmental TEM can be operated at atmospheric pressure^{104,146–150}. Regardless of applied pressure, a possible obstacle associated with TEM is the electron beam damage. Energetic electrons heat the particles locally, which might induce further particle sintering. The practical solution is to reduce the electron current density and to carefully investigate the beam effect. On the other hand, some studies exploit the energetic beam to heat the particles locally and follow the dynamical behavior in situ^{151–154} (in these cases, temperature cannot be quantified and imaging is performed in vacuum).

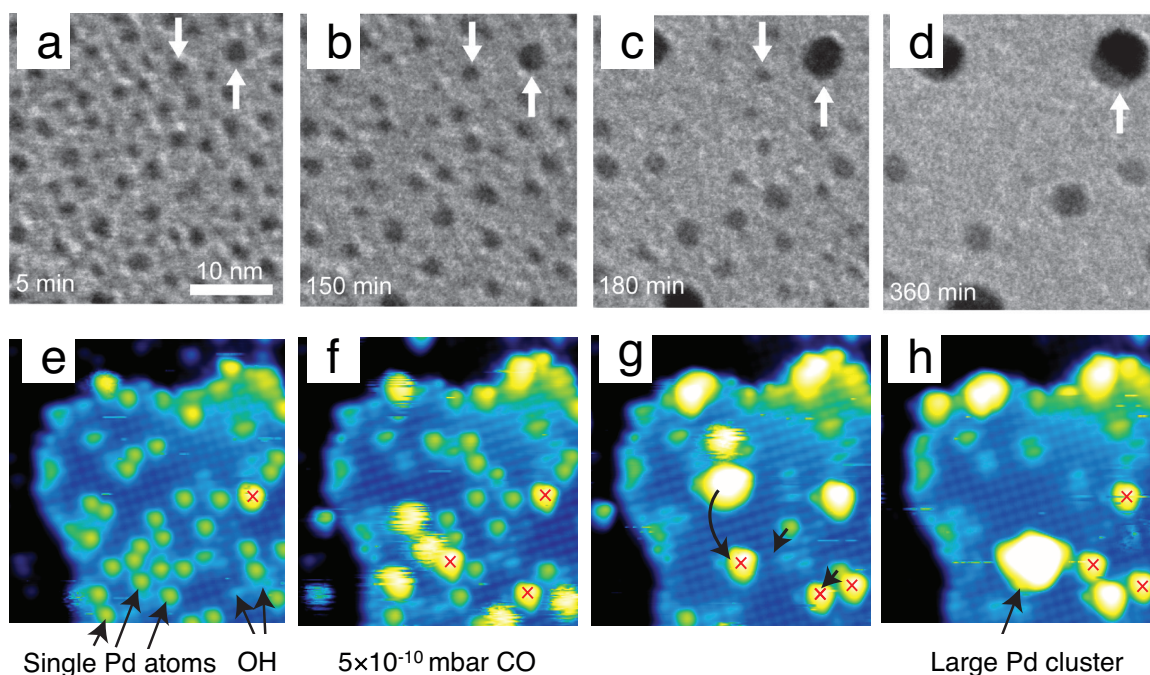


Figure 2.4. Examples of microscopy studies to monitor sintering processes (a-d) Time-lapsed TEM images of Pt/Al₂O₃ during exposure to 10 mbar air at 650 °C. Clearly, Ostwald ripening is observed as the dominant sintering mechanism. The series of images reveals that Pt nanoparticles are immobile, and larger particles grow in expense of shrinkage (and finally disappearance) of smaller ones. An example of a growing and a shrinking particle is denoted by the arrows. Modified with permission from ref. [116]. (e-h) Time-lapsed STM images of Pd/Fe₃O₄ during dosing with carbon monoxide at room temperature (time-span=110 min) shows particle migration and coalescence. Modified with permission from ref. [66].

Scanning tunneling microscopy (STM) can be employed to study sintering by obtaining topographic images of particles on a well-defined support^{80,166}. The technique is based on the quantum tunneling of electrons between a sharp metallic tip and a conductive surface. Often height of the particles (instead of diameter) is reported to avoid the effect of tip convolution and drift that can influence the lateral measurements. The high resolving power of STM allows the study of more fundamental surface processes such as monitoring the motion of single adatoms on the support⁶⁶. Design of high pressure (high implies pressures up to mbar range) STM setups has made it possible to study supported model catalysts in situ^{167,168}. Figure 2.4 (bottom row) illustrates the formation of large Fe₃O₄-supported Pd clusters by particle migration and coalescence induced by carbon monoxide at room temperature. Such studies are far from realistic catalyst systems and conditions, but elucidate surface processes, metal-support interaction, and the role of adsorbates at the nanoscale. Moreover, the STM results on well-defined surfaces can be compared with theoretical studies that are often based on simplified systems (e.g. well-defined particles on pristine oxide surfaces)³⁶. One inherent limitation is the inability of performing STM on

insulator supports like alumina and silica. In that case, alternative techniques such as atomic force microscopy (AFM)^{79,169,170} can be employed. One should note that if particle size and distribution is of interest, samples with narrow size distribution are more suitable to be studied, ensuring that the analyzed area represents the whole system.

Gas chemisorption measures the amount of gas (e.g. H₂) chemisorbed by the metal particles, which can be converted to a metal dispersion by assuming a specific adsorption stoichiometry^{155,156}. This stoichiometry is defined as the ratio of the number of molecules adsorbed per surface metal atom. In hydrogen chemisorption experiments, dispersion is normally determined by assuming a 1:1 ratio of H/Pt. However, unlike TEM where only local information can be obtained, gas chemisorption gives a global surface area value, from which an average particle size can be calculated assuming regular (e.g. spherical) and monodisperse particles.

X-ray diffraction (XRD): Average particle size is estimated by considering line broadening of the XRD reflections and applying the so-called Scherrer formula, $D = k\lambda/[\beta\cos(\theta)]$, where k is a dimensionless shape factor, λ is the X-ray wavelength, β is the width of the X-ray diffraction peak, and θ is the Bragg angle¹⁵⁷. However, very small particles might not be detected and for more precise calculation, the Scherrer formula should be modified for specific crystallite shape and the size distribution¹⁵⁷.

Extended X-ray absorption fine structure (EXAFS) is a synchrotron-based technique that estimates not only the size of small particles (~1 nm) at a given temperature and atmosphere, but also the geometric structure of nanoparticles^{158,159}. Another advantage of EXAFS is the possibility to provide chemical information of particles such as detection of adsorbates on nanoparticles and formation of oxide^{160,161} that is important for understanding processes such as sintering⁷³. EXAFS is an indirect way to study particle sintering where average size and shape of the particles are estimated based on parameters such as average coordination number. This method is more accurate in determining the size of smaller metal clusters (~100-1200 atoms)¹⁵⁸.

Small angle X-ray scattering (SAXS) can provide reliable results for sufficiently homogeneous samples based on the evaluation of an ensemble of particles^{157,162}. SAXS is a photon in-photon out experiment, thus there is almost no constraint on pressure and gas environment. Typically, SAXS requires synchrotron light and can provide time-resolved information¹⁶³⁻¹⁶⁵.

Indirect nanoplasmonic sensing (INPS) is an optical method¹⁷¹ that is used in this thesis to monitor Pt sintering on flat alumina and silica supports. A detailed description of the technique is provided in section 4.1. INPS enables monitoring of particle sintering kinetics with high time resolution under realistic conditions. The main constraint is that a complementary method is required to translate the obtained signal to a sintering descriptor (e.g. average diameter or particle density). Nevertheless, the technique allows for high throughput real time operando measurements of screening type. The other advantage is the use of a non-invasive probe (near-visible light), which does not interfere with the sintering process and that is compatible with operando conditions. In addition to model catalyst, INPS is proven to be useful in probing particle sintering supported on a mesoporous support that resembles commercial catalysts (Paper III).

To conclude, one should note that each tool gives information at different time and length scale. Some are limited by the choice of catalyst type and/or the applied sintering conditions. Table 1 briefly compares the techniques discussed above.

Table1. Summary of the described techniques for sintering studies.

Technique	Scale	Catalyst type	Main advantage(s)	Main Limitation(s)
Chemisorption	Global	Model and real	Realistic conditions	Hard to obtain particle size distribution
XRD	Global	Model and real	Realistic conditions	Small particles might be overlooked
SAXS	Global	Model and real	Realistic conditions	Synchrotron is needed
EXAFS	Global	Model and real	Realistic conditions, Shape & chemical Information	Synchrotron is needed, Not precise for particles > ~ 4 nm
TEM	Local	Model and real	Direct way to observe particles	Pressure limitation, Possible beam damage
STM	Local	Model (single-crystal)	Detailed mechanistic view	Pressure limitation, Insulator support cannot be studied
INPS	Global	Model (not single-crystal) and real	Realistic conditions, simple setup	Needs a complementary method to quantify the data

Sample Fabrication

In this thesis, Pt nanoparticles are deposited on either INPS sensor chips or TEM windows. This chapter describes the hole-mask colloidal lithography method that is used to fabricate the INPS sensors and alumina nanocones. It follows a description of the preparation of model catalysts and realistic catalysts and deposition of support material, as well as evaporation of Pt particles. In the last part, the structure of TEM window is described.

3.1. Hole-mask colloidal lithography

In Paper 1, INPS sensor chips featuring gold nanodisks (diameter of 80 nm and height of 20 nm) on glass substrate are used. They are fabricated using hole-mask colloidal lithography (HCL)¹⁷², followed by gold deposition. HCL is a bottom-up lithography method that is based on the self-assembly of charged polystyrene particles to produce the hole-mask. The sensors are fabricated in the MC2 cleanroom at Chalmers. The different process steps (Figure 3.1) are explained below.

(a) The process starts with spin-coating a thin PMMA layer (~300 nm) onto the glass substrate, followed by 10 minute hot plate baking at 170 °C to evaporate remaining solvent. To make the surface hydrophilic for the next steps, the sample is treated in oxygen plasma for five seconds (ashing). Polydiallyldimethylammonium chloride (PDDA) diluted to 0.2 % in deionized water is pipetted on the PMMA and forms a positively charged monolayer, followed by rinsing with deionized water and nitrogen blow-drying. Thereafter, negatively charged polystyrene (PS) colloids diluted to 0.2 % in deionized water are pipetted on the surface (about 1 minute incubation time), followed by rinsing and blow-drying. Since the surface and PS particles have opposite

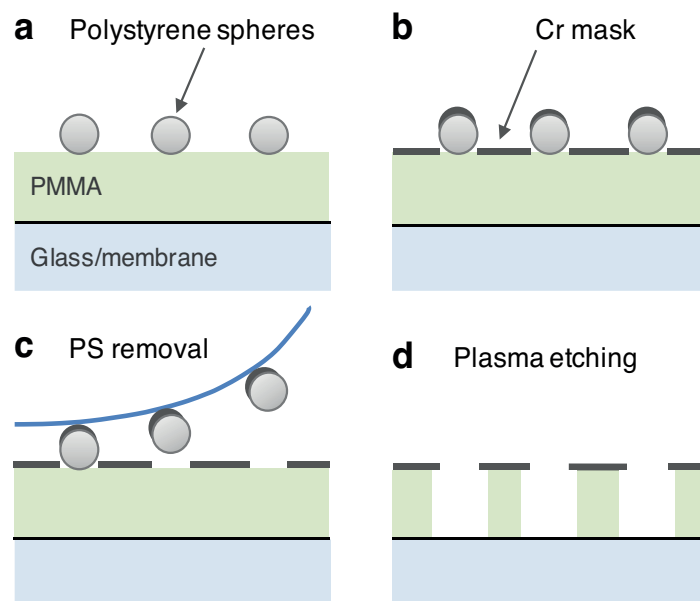


Figure 3.1. The key steps in hole mask colloidal lithography. See the text for a detailed explanation of each step.

charges, PS particles stick to the surface and maintain some distance by repelling each other. The result is a quasi-random arrangement of particles on the surface. The density of particles on the surface can be tuned by the PS colloid concentration, while the interparticle distances can be decreased by adding salt (e.g. NaCl) to the colloidal solution to screen surface charge. The average diameters of PS particles used were about 80 nm (Paper I and IV) and 140 nm (in Paper III).

(b) The metallic mask (e.g. 20 nm Chromium) is evaporated on the sample surface by a Lesker PVD 225 evaporator. The basic principle of e-beam evaporation is described in section 3.2.2.

(c) The polystyrene particles are removed by tape stripping. On the thin fragile membranes, however, the PS beads are removed by a wet tissue that is gently placed on the sample surface. This leaves arrays of circular holes in the metal mask on the PMMA surface.

(d) The last step in producing the mask is to etch the PMMA through the holes by oxygen plasma etching. The amount of undercut (see the Figure) can be changed by the etching time. My samples are etched for 5 minutes.

At this point, we are able to grow the desired nanostructure through the hole-mask. To fabricate gold sensor particles (Paper I and III), a gold film of 20 nm thickness is e-beam evaporated (Figure 3.2 a). Evaporation is a directional

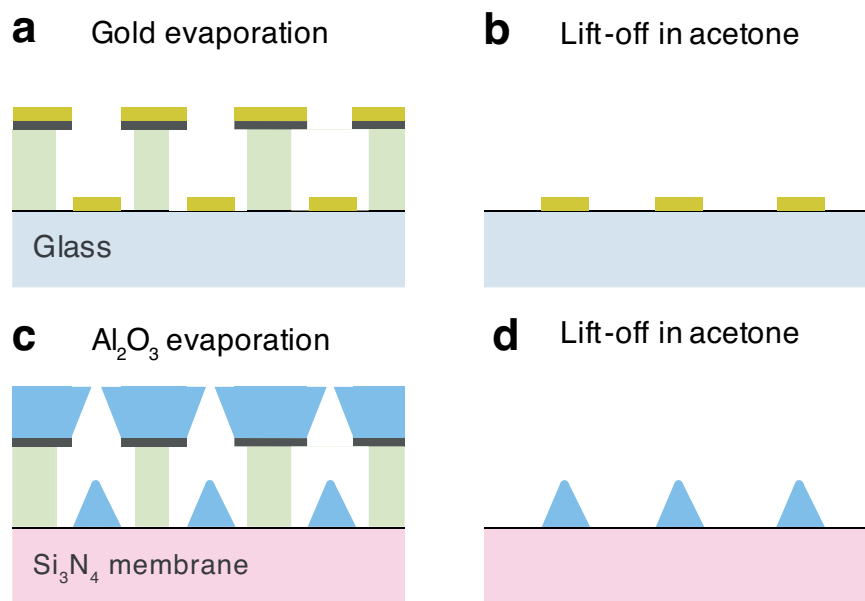


Figure 3.2. Deposition of (a,b) gold nanodisks and (c,d) alumina nanocones through the hole-mask.

deposition method, thus gold nanodisks with diameter of the size of the holes (ca. 80 nm in Paper I and ca. 140 nm in Paper III) and height of 20 nm are formed on the glass substrate without any contact to the PMMA. In the last step, the PMMA layer and the deposited layers on top are lifted-off in acetone, leaving only the gold nanodisks (i.e. sensor particles) on the surface (Figure 3.2 b).

The same procedure is applied in Paper IV to fabricate nanocones on a TEM membrane (Figure 3.2 c,d). In this case, an alumina film of 120 nm thickness is deposited using an AVAC HVC600 e-beam evaporation system. During evaporation, the material is deposited on the rim of the mask and the holes shrink gradually and are eventually closed¹⁷³. This results in formation of (truncated) cones. Finally, the residual materials are lifted-off by dissolving the PMMA in acetone.

To stabilize the sensor chip, the gold nanodisks are heat treated to assure that their shapes are retained during high temperature experiments (note that the change in the particle shape induces a spectral shift in INPS measurements). Figure 3.3 shows the effect of heat treatment (5 hours at 800 °C) on the gold nanodisks where they become faceted and attain hexagonal shape. Upon the shape change, the plasmon peak wavelength of particles is notably shifted, which can be seen from the sample color after the heat treatment.

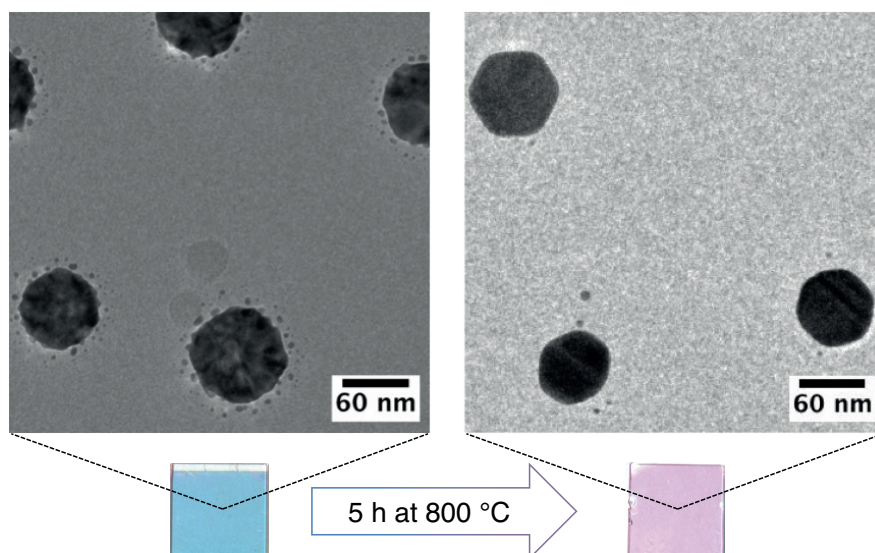


Figure 3.3. Gold nanodisks are heat treated to become thermally stable. TEM image and the corresponding sensor chip shows gold nanodisks (left) as prepared, and (right) after 5 hours heat treatment at 800 °C.

3.2. Fabrication of model catalysts

Model supports are deposited on the gold sensor particles (Paper I) and TEM membranes (Paper I, II and IV) by means of sputtering and plasma-enhanced chemical vapor deposition (PECVD). Oxide layers are then heat treated for 36 hours at 615 °C to become stabilized (e.g. in terms of density and refractive index) for INPS measurements. As a last step, Pt catalyst particles are thermally evaporated on the support. The details of these processes are described below.

3.2.1. Support deposition

3.2.1.1. Plasma-enhanced chemical vapor deposition

In general, chemical vapor deposition (CVD) uses chemical processes to produce conformal thin films (i.e. no thickness variation along edges, steps, etc.). The substrate is exposed to the reactants (gas precursors) where the material of interest is chemically formed on the surface. In plasma-enhanced CVD (PECVD), a plasma produces energetic species that assist the gas phase reactions. Hence, it becomes possible to perform deposition at lower temperatures (between 200 °C and 400 °C) as compared to thermal CVD. To create the plasma, the reactant gases are introduced between two parallel electrodes. The heated electrode that supports the substrate is electrically grounded, while RF (radio frequency) power is applied to the top electrode (Figure 3.4 left). In this work, SiO₂ is deposited by PECVD (STS) using silane (SiH₄) and nitrous oxide (N₂O) as silicon and oxygen precursor, respectively.

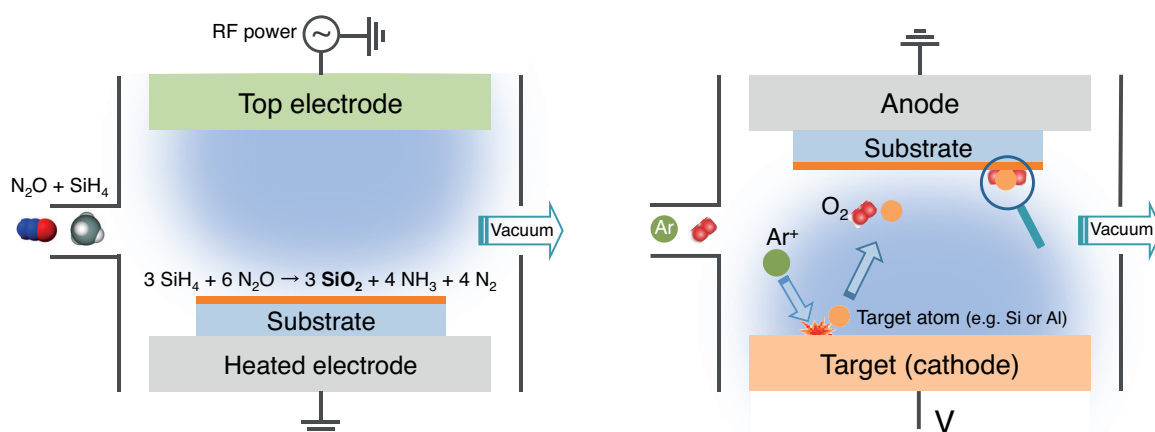


Figure 3.4. Schematic of (left) plasma-enhanced chemical vapor deposition (PECVD) of silica, and (right) sputter deposition of silica or alumina.

3.2.1.2. Sputter deposition

Sputter deposition is a physical vapor deposition (PVD) method that is used in this thesis to deposit alumina and silica. The schematic of the technique is shown in Figure 3.4. An inert gas such as argon is introduced to the chamber, and a plasma (including Ar ions) is created by applying DC or RF voltage between two electrodes. Energetic positive Ar ions are attracted to the cathode that is also the target material (e.g. Al or Si). The collisions between Ar ions and target material eject target atoms. This process is referred to as sputtering. The sputtered atoms move in all directions and hit the substrate. To deposit silica and alumina, reactive sputter deposition is used where oxygen- that is fed into the chamber- reacts with the sputtered Al or Si atoms to form the oxides. In the present study, silica and alumina were deposited by an FHR MS 150 machine.

3.2.2. Growth of Pt nanoparticles

Pt nanoparticles are grown by electron beam evaporation (AVAC HVC600 evaporator). To heat the target material (Pt), electrons emitted from the hot filament are accelerated (accelerating voltage of 3 to 40 kV), and directed to the Pt source with the help of a magnetic field (Figure 3.5). Since evaporation is carried out in a vacuum chamber, the Pt atoms (in vapor phase) travel within line of sight and finally condense on the substrate. The holder is water-cooled to avoid contamination that might result from evaporation of the holder material. The thickness of the deposited layer is monitored by quartz crystal microbalance (QCM), while the electron beam current controls the deposition rate. In our experiments, nominally 0.5 nm thick Pt was deposited at a rate of 0.5 Å/s, which results in the formation of irregularly-shaped Pt islands on the surface due to poor wetting. By heating the samples in Ar up to the aging

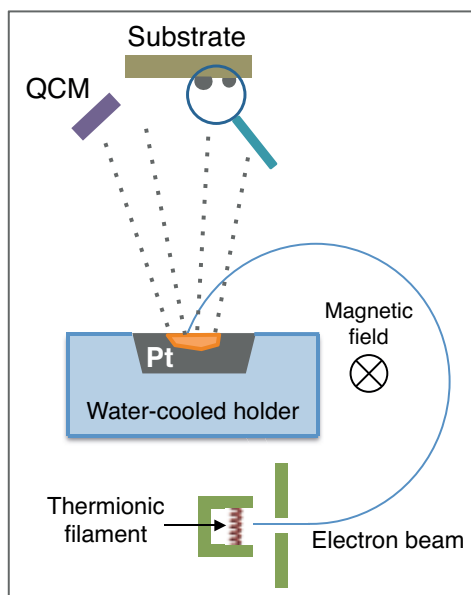


Figure 3.5. Basic principle of electron-beam evaporation of platinum.

temperature (first stage in all of the experiments), the Pt islands are transformed into almost spherical particles with average diameter of about 3 nm.

3.3. Synthesis of Pt catalyst in a porous alumina support

Real catalysts are often prepared on porous supports to enhance the specific surface area. γ -alumina is one common support which has a surface area of about 200 m²/g. Specific surface area can usually be measured by the BET method based on the theory by Brunauer, Emmett, and Teller¹⁷⁴. The technique is based on physisorption of an inert gas such as Ar or N₂ on the surface at liquid nitrogen temperature. By counting the number of molecules that are needed to form a complete monolayer, the surface area can be estimated, provided that the surface occupied by each N₂ molecule is known (e.g. 0.162 nm² at 77 K)¹. Below, the preparation of a porous γ -alumina is discussed, which is followed by introducing the techniques to disperse the metal particles inside the pores of the support.

Aluminum oxyhydroxide (γ -AlO(OH)) or böhmite that is used in Paper III is an important precursor material to prepare γ -alumina. Böhmite can be phase transformed to γ -alumina through dehydration by heating (calcination) at typically around 500 °C^{175,176}. Generally, calcination at higher temperature results in lower surface area of the formed alumina, which is associated with decrease in the average pore size^{177,178a}. One study showed that air calcination of böhmite with initial surface area of 213 m²/g leads to formation of alumina with surface area of 135 m²/g^{178b}. In this case, most of the decrease in surface area occurred in the first 30 minutes, and after 2 hours the surface area was

stabilized. The temperature at which the phase transition occurs as well as the structure of the final γ -alumina depend on parameters such as crystallinity of böhmite¹⁷⁵ and calcination conditions¹⁷⁹. For example, it has been shown that hydrothermal (steam) treatments of böhmite results in alumina with more well-developed crystallinity and larger average pore sizes than dry treatments^{178b}.

Two main routes for dispersing particles on a porous support are precipitation and impregnation that is explained in ref. [180]. The impregnation technique (used in Paper III) involves direct contact between metal catalyst precursor solution (mostly inorganic metal salt) and the mesoporous support, which leads to pore filling due to capillary forces. This is followed by drying of the slurry that plays a role in the final distribution of catalyst particles. Finally, by a second calcination step, the metal complexes are transformed into active metal nanoparticles.

Impregnation procedures can be divided into wet and dry impregnation. The latter is also known as pore volume impregnation or incipient wetness impregnation. Wet impregnation is carried out with an excess amount of solution that is required to fill the pores of the support, whereas in dry impregnation, the amount of precursor solution is equivalent to the pore volume. Generally, dry impregnation has an advantage of reducing the waste of catalyst precursor and preventing deposition on the external surface of the catalyst.

One way to deposit the Pt/alumina washcoat layer on an INPS sensor chip, is to spin-coat a slurry containing a mixture of support and catalyst precursor. However, this approach resulted in formation of particulate Pt/alumina (in the size range of micrometer) that does not fully cover the gold sensor particles. To circumvent this problem, we thus chose to first deposit the porous support on an INPS sensor chip, and then fill the pores with the Pt precursor solution (Figure 3.6). The mesoporous γ -alumina support is obtained by spin-coating böhmite and calcining it at 650 °C for 1 hour to phase transform to γ -alumina (Figure 3.6 b). As a result, a homogeneous mesoporous support layer in direct contact with the gold sensor particles is obtained (Figure 3.6 c). Since only a tiny amount of solution is required to fill the pores of the thin layer (below 500 nm), it is difficult to estimate the volume, and therefore excess solution of Pt precursor (wet impregnation) is used (Figure 3.6 d). The sample is then spun to remove most of the excess solution. Thereafter, the sample is freeze-dried and calcined at 550 °C for 1 hour to form metallic Pt catalyst that is dispersed uniformly throughout the porous matrix of γ -alumina. Finally, the residual Pt islands that are formed over the support as a result of spinning are removed by Ar ion milling (Figure 3.6 e).

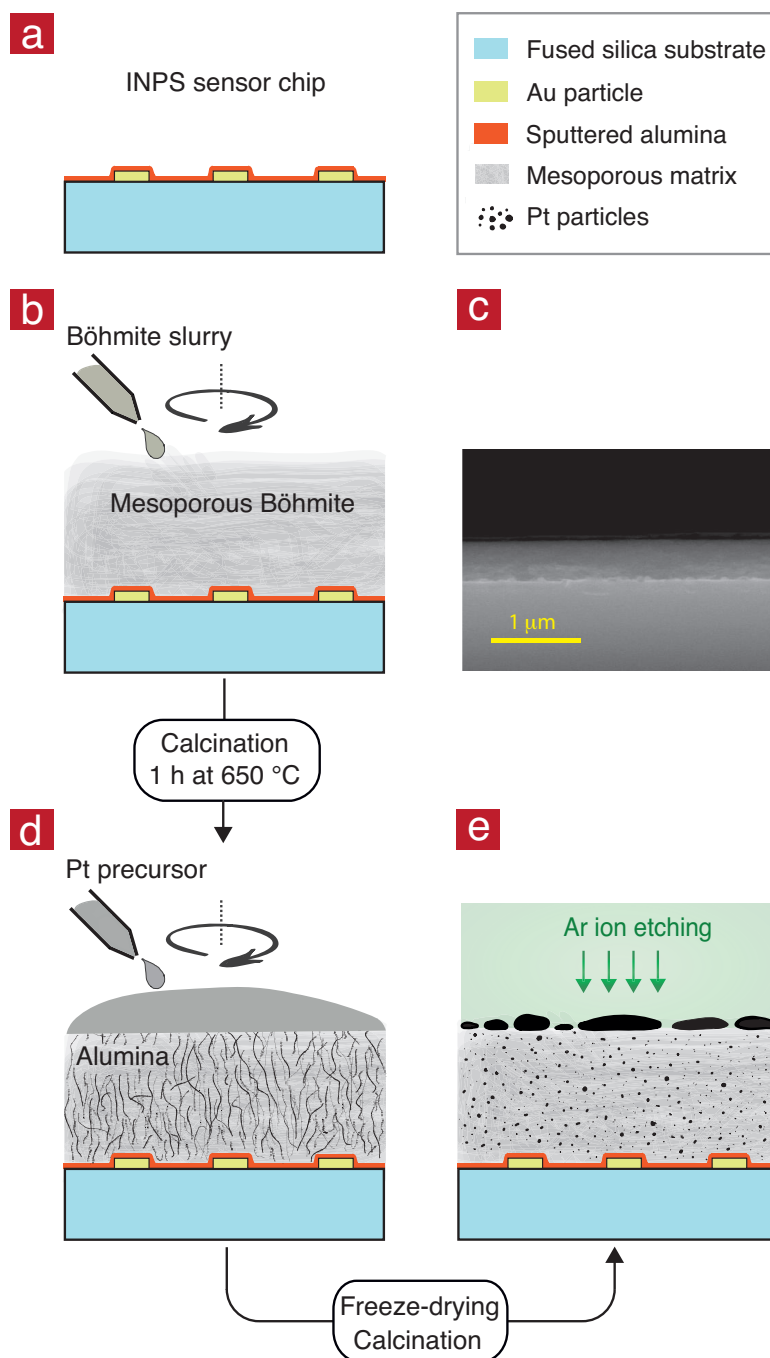


Figure 3.6. Key steps in the fabrication of Pt-impregnated mesoporous alumina on an INPS sensor chip. (a) Cross-section through an INPS sensor chip with thin sputtered alumina spacer layer. (b) Spin-coating of the böhmite precursor that is followed by calcination for phase transformation to γ -alumina. (c) Cross-sectional environmental SEM (ESEM) image shows a uniform γ -alumina support layer with thickness of ca. 400 nm on a sensor chip. (d) Wet-impregnation of the γ -alumina washcoat with Pt catalyst precursor. (e) Ar-ion etching of the residual Pt on top of the support layer resulting from excess Pt precursor after spinning.

3.4. TEM samples

To perform TEM on a model catalyst, the support material and subsequently the Pt particles are deposited on TEM windows that consist of a 40 nm electron-transparent amorphous Si_3N_4 membrane¹⁸¹. The TEM windows in this study have been fabricated in the MC2 cleanroom at Chalmers by the different steps including growth of Si_3N_4 , patterning by photolithography, and chemical etching of silicon. The structure of such TEM windows is illustrated in Figure 3.7. The thickness of the membrane influences the resolution of the imaging due to diffuse scattering of electrons by the nitride layer. The silicon nitride thickness in our windows is 40 nm, which adds notable weight to the background mass-thickness. Therefore, it is difficult to estimate the size of small Pt nanoparticles (< 1 nm) due to inadequate contrast with respect to the layers beneath, namely, 10 nm support material and 40 nm silicon nitride membrane. The 40 nm thickness has been chosen to obtain fairly high yield (around 70 %) in fabrication of TEM windows¹⁸¹.

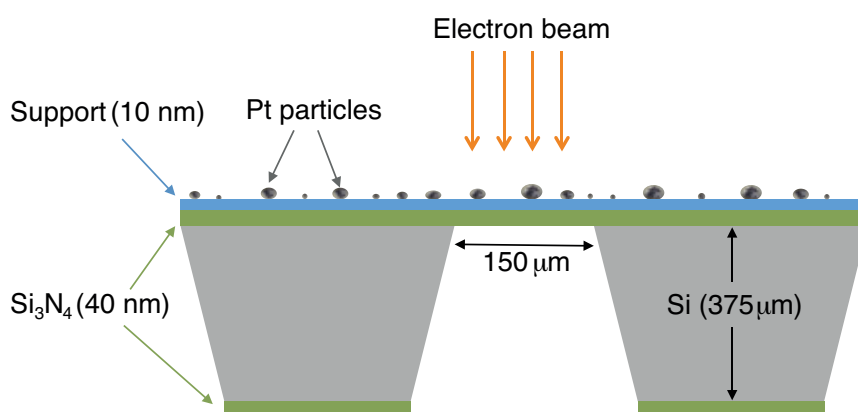


Figure 3.7. Schematic of TEM window, on which support material and Pt particles are evaporated. Note that the dimensions are not to scale. Adopted from ref. [181].

Characterization Techniques

4.1. Nanoplasmonic sensing

In Paper I and III, indirect nanoplasmonic sensing is employed to follow Pt nanoparticle sintering in operando on different catalyst systems and in different aging conditions. This section introduces light interaction with metal nanoparticles, and describes how one can use this for sensing purposes. Finally, the applicability of this sensing platform to monitor particle sintering is demonstrated.

4.1.1. Optical properties of metal nanoparticles

Since long time ago, glassmakers have exploited the properties of metal nanoparticles to stain glass. For example, colloidal suspensions of gold and silver particles produce ruby red and yellow, respectively, which differs from their bulk color. Figure 4.1 shows the light transmission through stained glass windows. The first scientific observations of light interaction with small metal particles were made by Faraday¹⁸². He synthesized colloidal gold particles by reducing gold chloride with phosphorous in water (Figure 4.1 b), and realized that the color of the colloidal suspension can be altered by varying the size of its constituent gold particles. The color variation due to the difference in particle size or shape is shown on a state-of-the-art nanofabricated sample in Figure 4.1 c.

When light shines on a metal particle of a size comparable to the wavelength of light, the conduction electrons of that particle can oscillate collectively in resonance with the incoming light – this is called *localized surface plasmon resonance*, LSPR¹⁸³ (Figure 4.2 a). The LSPR has two consequences of relevance

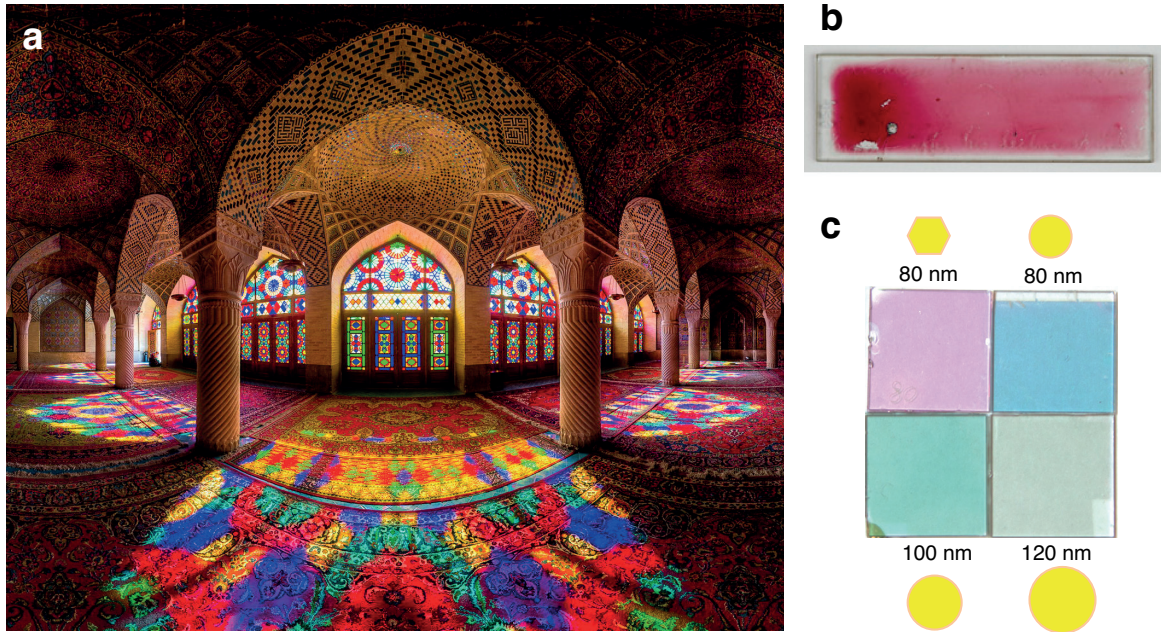


Figure 4.1. Interaction of light with small metal particles differs from their bulk counterpart. (Left) Light shines through stained glass windows in the Pink Mosque located in Shiraz, Iran. (Top right) Gold colloids on a microscope slide that was prepared by Faraday. Copyright of Whipple Museum of the History of Science. (Bottom right) Gold particles with different size/shape nanofabricated on a glass substrate. Clearly, different size/shape of the particles give rise to significant changes in the color.

for the work presented in this thesis, namely the appearance of a peak at a specific wavelength, λ_p , in the optical far field extinction (sum of scattering and absorption) spectra (Figure 4.2 b), and an enhanced electromagnetic near field around the particle (Figure 4.2 c). If the wavelength of the plasmon peak lies in the visible region of the electromagnetic spectrum, parts of irradiated white light are absorbed and scattered by the particle, which leads to the colors seen in Figure 4.1. The spectral position of the plasmon peak (i.e. the resonance frequency of the collective electron oscillation) depends on the composition, the shape and size of the particle, as well as the dielectric environment around it. The latter is the basis of nanoplasmonic sensing that is described in the next section.

Properties of plasmonic particles (e.g. size/shape) can be correlated to their optical response by techniques that can be performed on single particle level¹⁸⁴. Gustav Mie was first to theoretically describe how small metal spheres ($D \ll \lambda$) absorb and scatter light by analytically solving the Maxwell's equations (see ref. [185] for derivations). However, as the shapes of the plasmonic entity become more complicated, using numerical methods is more desirable¹⁸⁶. Finite-difference time-domain (FDTD) electrodynamic simulation is one of these methods that is used in Paper I.

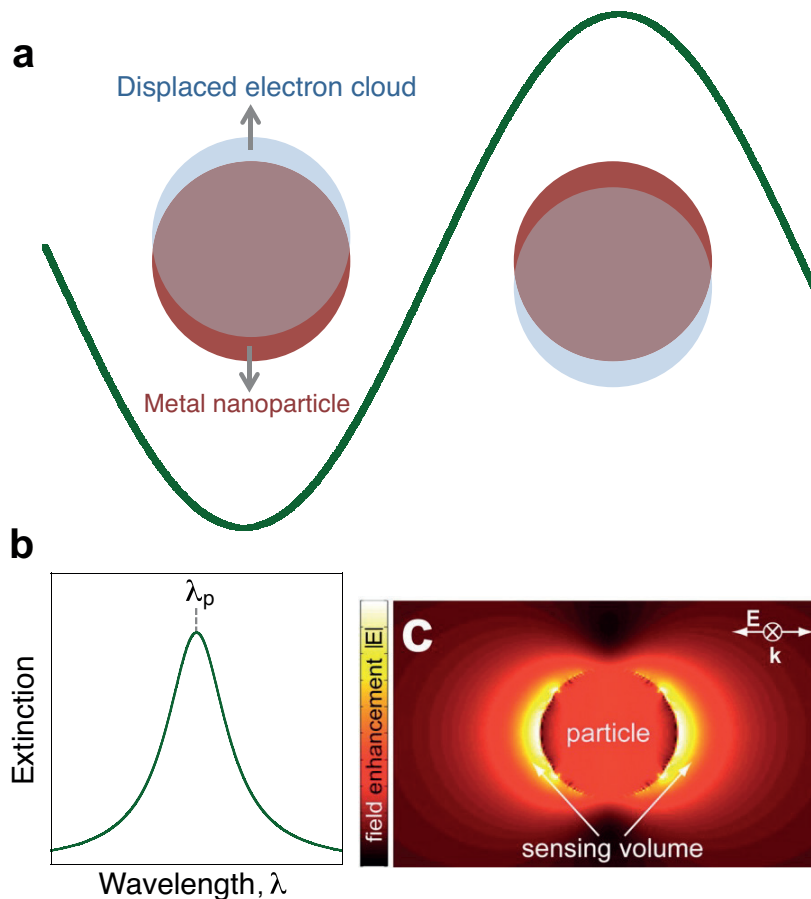


Figure 4.2. Interaction of light with metal nanoparticles. (a) Light with appropriate wavelength can excite the free electrons of a metal nanoparticle, and cause them to oscillate coherently and in resonance. This resonance gives rise to two effects: (b) a distinct peak in far field extinction spectra at the resonance wavelength, λ_p , that results from strong scattering and absorption of light, and (c) an enhanced electromagnetic near field around the particle. Field enhancement around a gold nanodisk (diameter = 80 nm and height = 20 nm) illuminated at the LSPR wavelength is simulated by the finite-difference time-domain (FDTD) electrodynamic simulation method. Panel c is reprinted with permission from ref. [171]. Copyright American Chemical Society 2012.

4.1.2. Sensing principle

The dependence of the plasmon peak wavelength (λ_p) of a spherical particle on the refractive index of the surrounding medium (n) is expressed by

$$\lambda_p = \lambda_b \sqrt{2n^2 + 1} \quad (4.1)$$

where λ_b is the wavelength corresponding to the plasma frequency of the bulk metal¹⁸⁵. Approximately, there exists a linear relationship between the peak position and the medium refractive index. Figure 4.3 demonstrates the color change of gold nanoparticles illuminated with white light after pipetting a few

drops of ethanol onto them. The reason is that, according to equation (4.1), varying the refractive index around the particles leads to the shift in plasmon peak wavelength, and consequently the change in color. This dependency allows plasmonic particles to “sense” the local changes in refractive index of their surrounding. In nanoplasmonic sensing, the readout is often a spectral shift of the peak wavelength ($\Delta\lambda_p$) that can be measured by a spectrometer with high spectral¹⁸⁷ and temporal resolution (in the millisecond range). Typically, the bulk refractive index sensitivity value, S , of a plasmonic-based sensor is reported in LSPR peak shift per refractive index unit.

$$S = \Delta\lambda/\Delta n \quad (4.2)$$

This value depends on the material, as well as size and shape of nanoparticles¹⁸⁵.

Nanoplasmonic sensing has been widely employed in biological analyte detection¹⁸⁸, and more recently in materials science^{189–191}, including catalysis studies^{171,192,193}. It can be performed on ensembles of plasmonically active particles, as well as on a single nanoparticles^{194,195}. Among many plasmonic metals, gold and silver are chosen the most due to their especially suitable

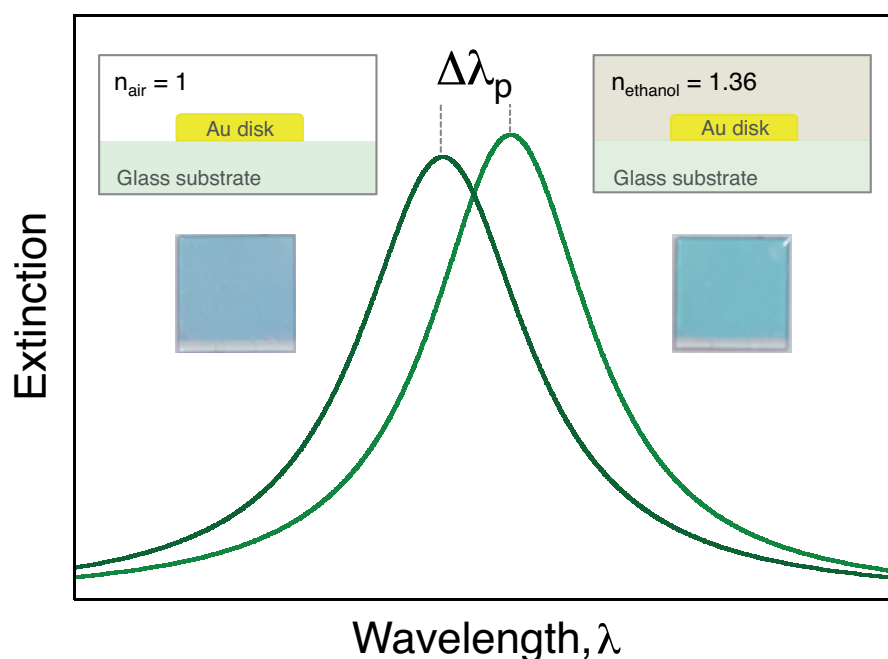


Figure 4.3. Basic principle of nanoplasmonic sensing. The sample to the left is comprised of an ensemble of gold nanodisks (diameter = 80 nm and height = 20 nm) on a glass substrate in air, whereas to the right, the same sample is covered by ethanol. Because of the change in the refractive index around the particles, the plasmon peak is shifted and causes color change (see equation 4.1). This sensitivity towards refractive index changes is the basis of nanoplasmonic sensing. In this example, the spectral shift is large enough that it can be observed by the naked eye.

permittivities (low losses in the visible spectral range). Although silver particles exhibit sharper peak and greater sensitivity, gold particles are favorable if chemical stability is required. In this context, it should be noted that the plasmonic sensor nanoparticle can detect the refractive index changes only within a limited region (extending a few tens of nanometers from the particle surface), which in most cases is advantageous. This region is called the *sensing volume*, and it corresponds to the enhanced electromagnetic field around the particle that is exponentially decaying away from the particle surface (Figure 4.2 c). The specifics of the field enhancement and the sensing volume depend on the metal, particle geometry, and the dielectric environment of particle.

4.1.3. Indirect nanoplasmonic sensing

To monitor nanoparticle sintering in situ, the plasmonic sensing described above can be performed indirectly, which means that the plasmonic gold nanosensors and the probed material (catalyst nanoparticles) are separated by a thin oxide spacer layer (Figure 4.4). The spacer layer should be thin enough that the studied material is still located within the sensing volume of the sensor particles. This specific sensing platform is referred to as indirect nanoplasmonic sensing (INPS)¹⁹⁰. The spacer layer protects the gold particles from harsh environment, and prevents alloying between the catalyst particles (e.g. Pt) and the gold sensors at high temperature. When sintering on a flat support is of interest, the oxide layer can also serve as a support material for the catalyst particles (Figure 4.4 a-d). In paper I, we use 10 nm thick alumina and silica layers as model supports. Depositing such a layer with a refractive index larger than air causes the LSPR peak to red-shift. In addition, the support refractive index influences the intensity and profile of enhanced field around the gold sensor particles and consequently the sensitivity¹⁹⁶. This problem is addressed in Paper I by performing FDTD simulations, where we find that the effect of different support (silica or alumina) can be cancelled out by normalizing the peak shift by the corresponding refractive index value.

The INPS setup (Insplorion X1 flow reactor system, Insplorion AB, Göteborg, Sweden) consists of a quartz flow reactor with optical access for transmission measurement, and is equipped with a heating coil and mass flow controllers to provide the desired aging conditions (Figure 4.5 left). The INPS sensor with the deposited Pt is placed in the reactor, and is then exposed to the sintering temperature and desired gas conditions. Rearrangement of the Pt particles due to sintering changes the effective refractive index around the sensor gold particles, and hence, causes a shift in the plasmon peak ($\Delta\lambda_p$). The spectra are recorded by a fixed-grating spectrometer with high temporal resolution

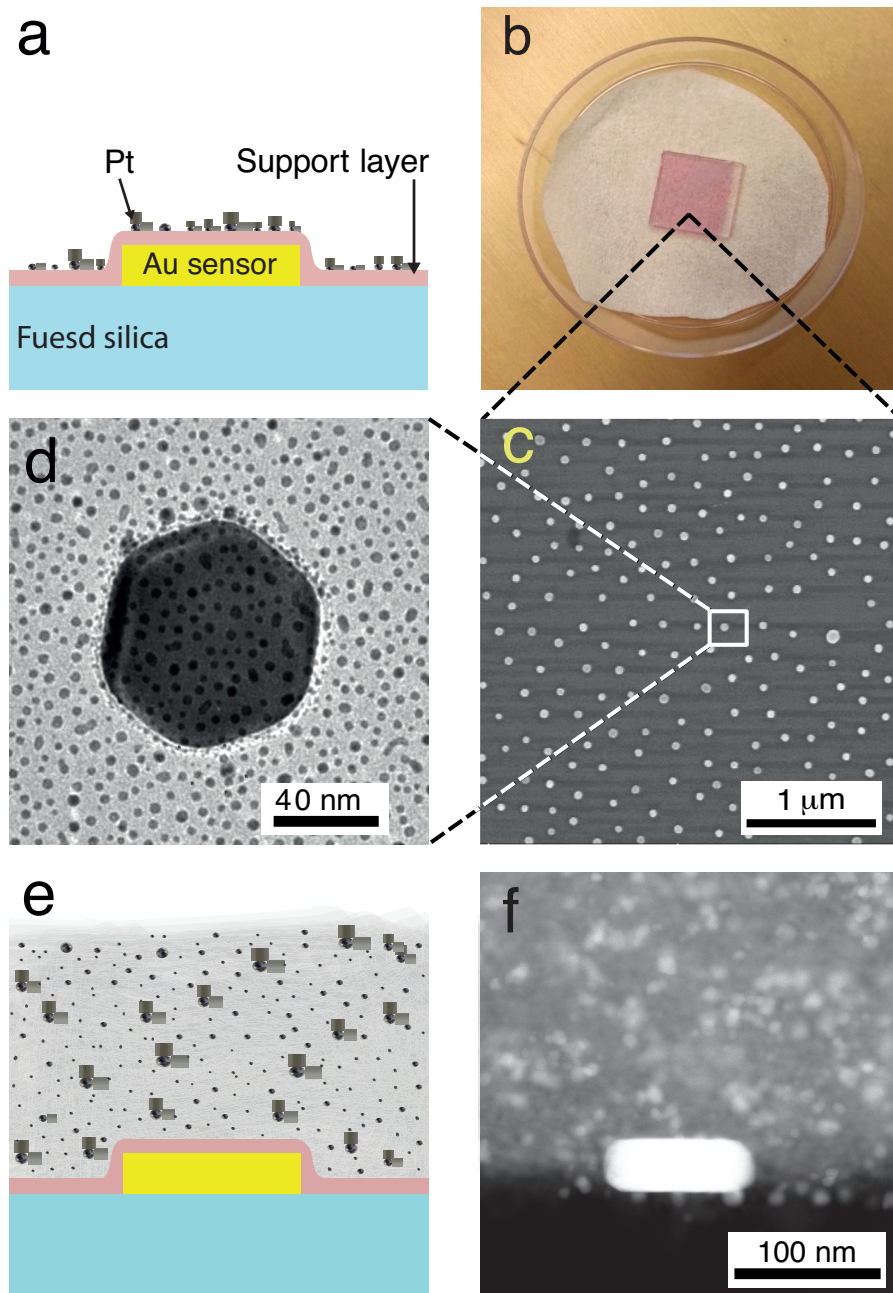


Figure 4.4. Indirect nanoplasmonic sensing platform. (a) The INPS sensor consists of an array of Au nanoparticles fabricated on a glass substrate. The particles are covered by a thin layer of oxidic catalyst support material, on which the Pt catalyst particles are deposited. (b) 1x1 cm INPS sensor. (c) Environmental SEM image of plasmonic gold sensor nanoparticles covered with a 10 nm thick silica catalyst support layer. (d) TEM image of as-deposited Pt on a single gold sensor nanoparticle covered with a 10 nm thick silica catalyst support layer. Side-view (e) schematic illustration and (f) Scanning TEM (STEM) image of Pt-impregnated mesoporous alumina on an INPS sensor chip.

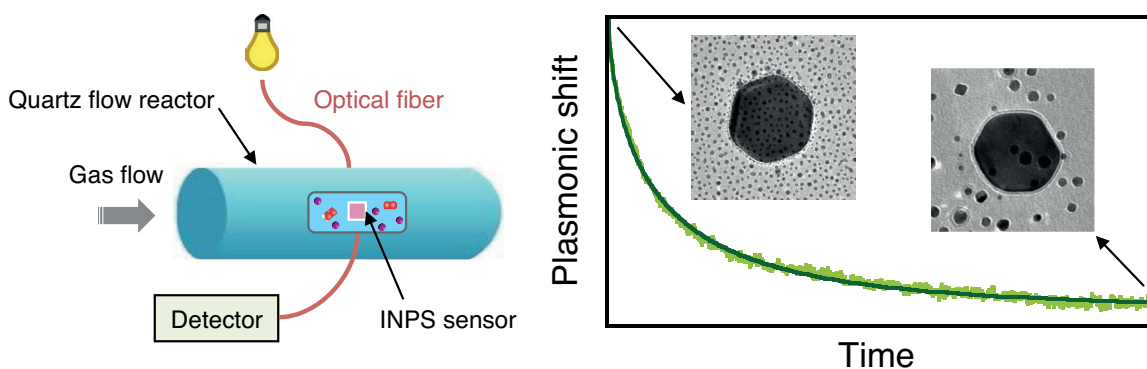


Figure 4.5. Real time monitoring of nanoparticle sintering by indirect nanoplasmonic sensing (INPS). (Left) Schematic of the INPS setup; the INPS sensor decorated with Pt particles is exposed to the desired gas environment at high temperature in a quartz flow reactor, through which the optical extinction measurement is performed. (Right) Plasmonic peak shift reflecting the sintering of Pt nanoparticles on the INPS sensor. The TEM images show a single gold sensor with Pt before exposure to 4% O₂ in Ar at 600 °C, and after 12 h in the gas mixture. The area of TEM images is 160 × 160 nm².

to obtain operando high-resolution kinetic data (Figure 4.5 right). The TEM images in the plot show the Pt particles on a gold sensor before exposure to the sintering conditions, and after 12 h of sintering. Clearly, the mean particle size increases, in general agreement with the INPS measurement.

Note that the plasmonic signal, i.e. the spectral shift of the peak wavelength, does not directly express the extent of sintering quantitatively. Thus, the experimentally measured plasmonic signal has to be converted to a sintering descriptor such as the mean particle diameter, $\langle D \rangle$ ¹⁹⁷. To do that, ex situ intermittent TEM can be used to determine the mean diameter of sintered particles after certain time intervals, which then is correlated to the measured plasmon peak shift after the same time intervals. Following this procedure, the plasmon peak shift, $\Delta\lambda_p$, (e.g., in Figure 4.5 right) can be translated to the mean particle size by an empirical calibration formula that relates $\Delta\lambda_p$ to $\langle D \rangle$ (details are provided in Paper I). By this translation, high (temporal) resolution quantitative kinetic data of the sintering process is obtained under realistic conditions and can be considered for further analysis. It should be noted that the sensitivity of the technique (signal shift per Pt particle size change) decreases when the particle size increases, which can be rationalized as follows; when Pt particles grow larger they extend further away from the Au sensor surface where the field enhancement is weaker, and thus a smaller peak shift per unit size change is expected. Nevertheless, there is almost no lower size limit for detecting changes in the nanoparticles, as has been shown on the example of size-selected Pt clusters of 22 and 68 atoms⁵⁰.

4.2. Transmission electron microscopy (TEM)

Similar to the optical microscope, the *transmission electron microscope* (TEM)¹⁹⁸ forms a two-dimensional image of the sample. The main difference is that in electron microscopy, accelerated electrons (instead of visible light) with much shorter wavelength are utilized to achieve higher resolution. According to the de Broglie equation, $\lambda = h/p$ (h is Planck constant and p is the electron momentum), electrons with higher energy have smaller wavelength that enables probing with higher resolution. Thus, to ultimately reach atomic resolution, the electron beam is typically accelerated with 80 kV to 300 kV. Due to strong electron-sample interaction, the sample should be thin enough for electron transmission. The required thickness depends on the sample nature and desired resolution/contrast.

Figure 4.6 (left) shows a schematic illustration of a TEM setup that consists of the electron gun, the imaging system (lenses), and a display system. Two kinds of electron sources are used; thermionic and field emission. Thermionic sources are made from a material with high melting point and low work function that produces electrons by heating it, whereas in a field-emission source, a large electric potential between the source (e.g. a tungsten filament) and an anode creates electrons. The electron gun focuses the electrons emitted from the source (thermionic or field-emission) to provide an intense beam

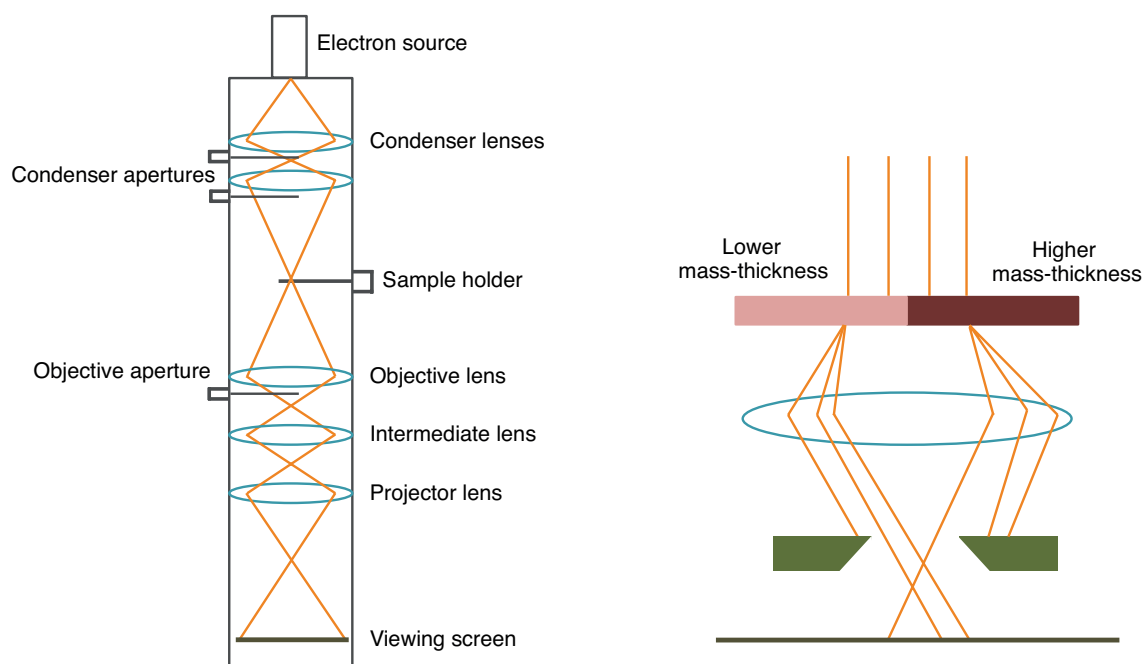


Figure 4.6. (Left) Schematic illustration of a TEM, and a simple ray diagram showing how the image is formed, and (right) scattering of incident electron beam by regions with different mass-thicknesses. Adapted from ref. [198].

of high-energy electrons. The minimum cross-section of the electron beam ahead of the source is called the cross-over that goes through the imaging system. The imaging system mainly consists of electromagnetic lenses (that can be considered as convex lenses) and apertures. The first condenser lens demagnifies the cross-over to a smaller spot size and the second lens enlarges this spot size. The condenser lens thus controls the amount of electron radiation illuminating the sample. The objective lens that is placed after the sample is used to focus and initially magnify the image. Further magnification is performed by the intermediate and projector lenses. The display system is a florescent screen that detects the transmitted electrons as well as a CCD camera. In Paper I and II, TEM is performed in the bright field mode where the contrast mainly arises from the diffraction-contrast and mass-thickness of the sample at the applied magnifications. Figure 4.6 (right) illustrates how an incident electron beam is scattered by regions with different mass-thicknesses. The higher mass-thickness region scatters the electron beam more strongly, hence a weaker beam is passed through the aperture and it appears darker. For that reason, Pt particles appear darker compared with alumina or silica support (Figure 4.5). For TEM imaging in this thesis, an FEI Tecnai G2 at an acceleration voltage of 200 kV is used, which is equipped with LaB₆ crystal as thermionic source.

In addition, imaging can be done in a mode called scanning transmission electron microscopy (STEM), in which a focused beam is scanned over the surface in a raster fashion. Unlike the conventional TEM mode, transmitted electrons are directly collected without undergoing to any lensing system below the sample. To achieve a high elemental contrast in STEM, a high-angle annular dark field (HAADF) detector can be used below the specimen. This detector excludes the electrons close to the optical axis and therefore vacuum (that does not scatter electrons) appears black, hence the name dark-field. The measured intensity is approximately proportional to the square of the atomic number (Z^2), which means elements with different atomic number can be distinguished easily. For that reason, HAADF-STEM (also called Z-contrast imaging) is used in Paper III and IV, where small Pt particles (high Z number) are located on thick layers of alumina (low Z number). In this work, STEM is performed using an FEI Titan 80-300 (operated at 300 kV) equipped with a field emission gun.

4.3. Scanning electron microscopy (SEM)

The probe in SEM is a focused electron beam that is emitted from an electron source (typically field-emission gun). Compared to TEM, the electrons possess much lower energy (0.1 to 30 kV), and therefore lower resolution is expected. The beam is focused on the sample by two or more electromagnetic lenses and is scanned over the desired area by the scan coils. The impinging electrons penetrate into the sample within the so-called interaction volume that depends on the acceleration voltage and the sample nature (mainly the mean atomic weight). Interaction of electron beam and sample atoms emits back various types of signals, which can be measured with specific detectors. In this work, two signals are used to construct an image, namely secondary electrons (SE) and backscattered electrons (BSE).

Secondary electrons originate from inelastic scattering of electron beam and sample. These low energy electrons (usually below 10 eV) mostly contain information from depths of few tens of nanometers from the surface (depending on the acceleration voltage and the material). Because of their low energy they cannot escape from deep inside the sample as they are reabsorbed by the material. Typically, when topographic information is of interest, SE becomes a useful signal to detect. On the other hand, BSE are created from elastic scattering, and thus they possess high energy and are emitted from deeper parts of the sample. Since the probability of elastic scattering corresponds to the Z (atomic weight) number, compositional contrast can be achieved. Figure 4.7 shows SEM images of Pt/alumina on gold sensor particles by detecting SE and BSE. Gold nanodisks and even small Pt particles are clearly visible

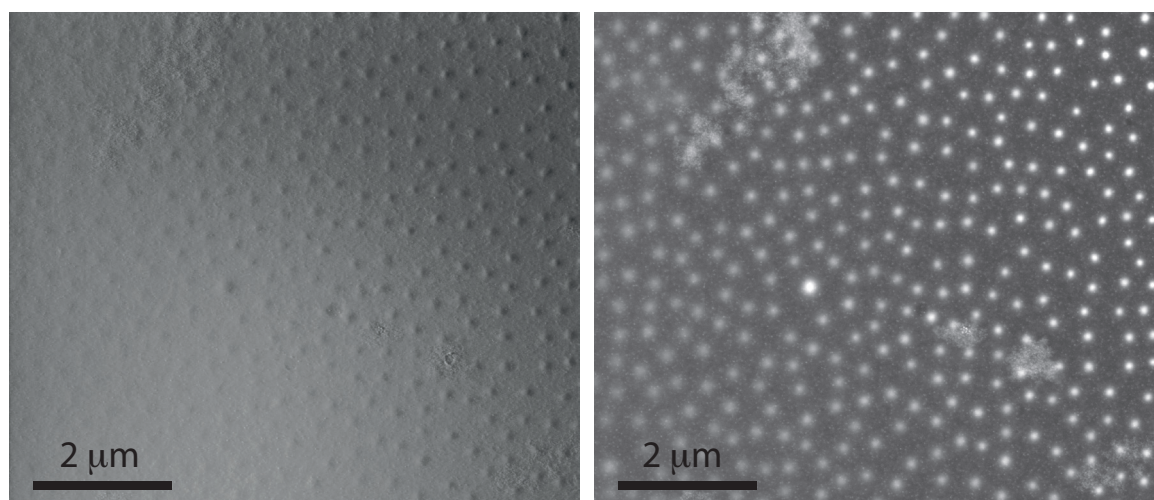


Figure 4.7. Environmental SEM images of Pt/alumina catalyst washcoat on an INPS sensor chip. These images are acquired simultaneously by using different detectors for (left) secondary electrons (SE) and (right) backscattered electrons (BSE).

thanks to the compositional contrast acquired by BSE (Figure 4.7 right), while topographic information is better resolved by SE (Figure 4.7 left).

SEM is used in paper III to image the washcoat layer (i.e. Pt-impregnated mesoporous alumina) on the INPS sensor chip at different stages of the fabrication and sintering processes. However, as the alumina support and the glass substrate are insulators, performing conventional SEM causes charge accumulation and consequently deterioration of the image quality. In order to overcome this problem, it is possible to coat the surface with a thin film of a conducting material (such as carbon or gold), or use SEM operated at lower vacuum. Following the second approach, we employ environmental SEM (ESEM) operated at 20 kV, where water vapor (pressure = 0.68 Torr) is used to neutralize the charge build up during the scan.

4.4. Ellipsometry

In Paper I, ellipsometry (J.A. Woollam M-2000) was performed to determine the refractive index of the support material (i.e. spacer layer of the INPS sensors). Figure 4.8 shows a simple schematic of the setup. Linearly polarized light is irradiated on the sample, and becomes elliptically polarized upon reflection. The reflected light passes through the rotating polarizer (i.e. analyzer) and reaches the detector where the amount of polarization, both in amplitude and phase, is determined. The polarization change depends on several sample properties, such as composition, refractive index, and thickness. By providing an estimate of the layer thickness, the refractive index is obtained through fitting to optical models. In our work, we deposited 50 nm-thick sputtered alumina and PECVD silica layer on a silicon substrate that was followed by 36 hours heat treatment at 615 °C. A thicker layer compared to the support layer on the sensor (10 nm) was deposited for these measurements to eliminate the effect of interface layer between silicon substrate and the oxide.

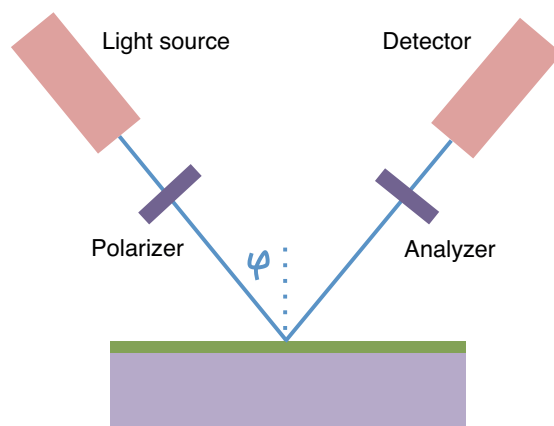


Figure 4.8. Schematic picture showing the principle of ellipsometry.

Summary of Results

Paper I

In Paper I, we present indirect nanoplasmonic sensing (INPS) as an operando tool that in combination with TEM allows the monitoring of Pt sintering kinetics on different supports and under different gas conditions with high time resolution. Previously, INPS has been used to explore sintering of Pt/SiO₂ in O₂ environment¹⁹⁷. Here, the flexibility of INPS to follow Pt sintering on different support materials and in different gas environments is demonstrated. Three different sintering experiments at 600 °C are considered, namely, Pt/Al₂O₃ in 4 % O₂, Pt/SiO₂ in 4 % O₂, and Pt/SiO₂ in 0.1 % NO₂. To understand the role of the support refractive index in the measured INPS signal, finite-difference time-domain (FDTD) electrodynamic simulations of the structures are performed. They reveal a linear relation between the change in the INPS signal and the support refractive index (RI). This enables direct comparison of the Pt sintering on different supports by scaling the data with the refractive index of the support (see Figure 5.1).

In this study, we also investigate the dependence of the sintering rate of a SiO₂-supported Pt model catalyst on the O₂ concentration (range: 0.05–0.5 %) by solely relying on the derived calibration formula for silica support in O₂ (red curve in Figure 5.1 b), which allows conversion of the INPS data to kinetic curves that show the mean diameter evolution. Using this approach, we find a clear dependence of the sintering rate on the O₂ concentration that is in line with previous studies^{33,54,200}.

In conclusion, we find that INPS can be effectively applied to screen nanoparticle sintering with high time resolution and under realistic conditions on different

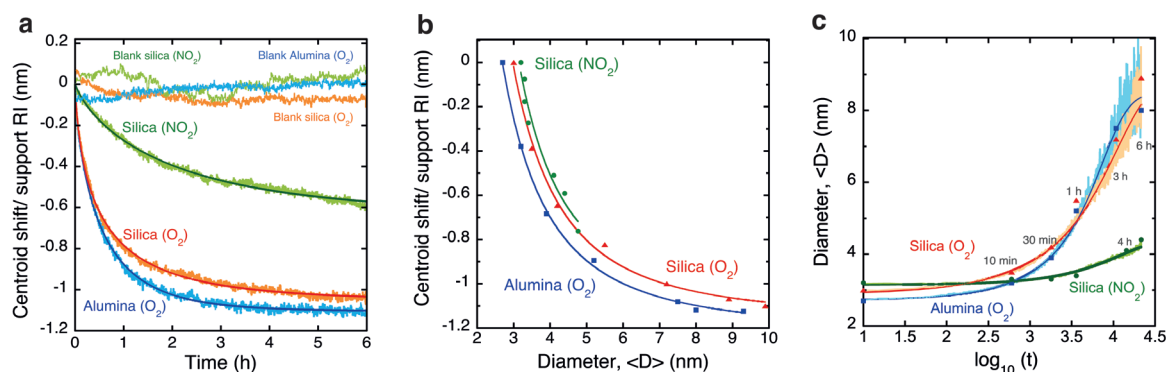


Figure 5.1. (a) INPS sintering curves scaled with the refractive index of the support layer. The solid lines correspond to an exponential function fitted to the raw INPS curves. Corresponding INPS traces of blank sensors (i.e. without Pt) exhibit a negligible centroid shift at the applied conditions. (b) Correlation between refractive index-scaled INPS centroid signal and mean particle diameter $\langle D \rangle$. An empirical calibration formula can be obtained by fitting a function of the form $\Delta\lambda = A + B\langle D \rangle^{-n}$ to the experimental points. (c) High resolution real time sintering kinetic data (solid lines) obtained by translating the centroid shift to mean particle size, $\langle D \rangle$, using the derived translation functions from the analysis in panel (b). The dark full lines correspond to fitted exponential functions to the raw data and serve as a guide to the eye. The discrete points show the mean particle diameter derived from TEM.

support materials and in different gas environments. At the same time, it is also important to note that one limiting factor of INPS in sintering studies is that the signal is not selectively/exclusively sensitive to the rearrangement of particles. In other words, also other processes that change the dielectric environment around the sensors give rise to a signal. Therefore, careful design of the experiments in combination with appropriate control measurements are critical to rule out other possible processes that give rise to the measured plasmon peak shift during a sintering experiment.

Paper II

The kinetic data obtained by INPS (Paper I) are based on an ensemble average of particles. Therefore more detailed information on the evolution of particles during sintering might be hidden in the average and thus not be resolved. Therefore, in Paper II, we analyze the particle size distributions (PSDs) of Pt particles on alumina, PECVD silica, and sputtered silica during sintering for up to 24 hours at 600 °C (time-resolved), and after 12 hours at 500, 550, and 600 °C (temperature-resolved) in 4 % O₂ in Ar by TEM, to elucidate the sintering processes in more detail. Two different types of silica support were chosen (deposited by two different chemical vapor deposition methods) to investigate if subtle differences in terms of support stoichiometry, surface roughness, etc. are important.

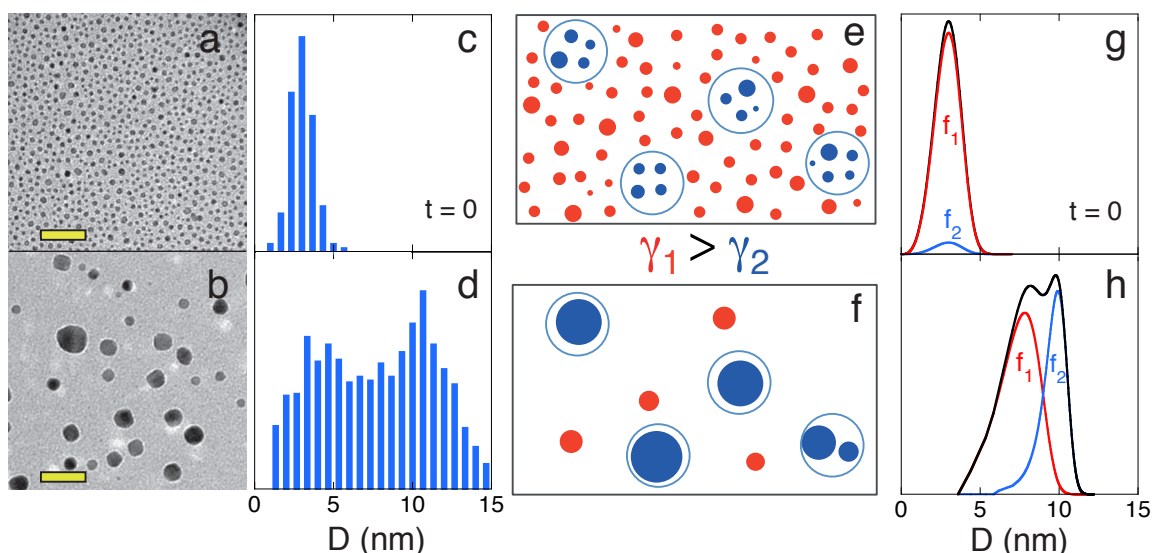


Figure 5.2. TEM images and corresponding PSDs of alumina-supported Pt particles (a,c) before oxygen exposure, and (b,d) after sintering in 4% O₂ in Ar at 550 °C for 12 hours. The scale bar: 30 nm. (e) Schematics of randomly distributed particles on a heterogeneous support including two types of patches with different metal-support interface energies ($\gamma_1 > \gamma_2$). (f) After sintering, larger nanoparticles are located mainly at patches of type 2 (with lower interface energy). (g,h) Calculated size distributions of particles at $t = 0$ and after sintering at 550 °C on the described surface. f_1 and f_2 correspond to PSDs on patches of type 1 and 2, respectively.

The initial PSDs (before exposure to oxygen) for all the cases are approximately Gaussian with a peak around 3 nm. As a common feature, transient bimodal distributions are observed for Pt sintering on all three supports. As an example, Figure 5.2 (a-d) shows TEM images and corresponding PSDs for Pt/alumina before oxygen introduction and after sintering for 12 h in 4 % O₂ at 550 °C. The observed bimodality in size distribution does not match the conventional theoretical predictions that assume a homogeneous support surface.

To explain our observations, we present a model that takes into account the support heterogeneity. The model assumes that the particles are randomly distributed on a surface that consists of two types of patches with different metal-support interface energy, γ (Figure 5.2 e,g). Ostwald ripening on this type of support can be explained qualitatively as follows; since the energy barrier for detachment of monomers from a region with stronger metal-support interaction (higher γ) is lower, the monomer detachment rate from these patches is higher compared to the patches with lower γ . Given enough time, the particles will be located primarily on the former regions (Figure 5.2 f). During this transition, bimodality in the particle size distribution is expected. This is shown in the calculated PSDs based on interface-controlled Ostwald ripening (Figure 5.2 h). Conceptually, it can also be shown that similar distribution is expected in the case of particle migration.

Finally, in this paper, we also discuss the difficulty of deducing the main sintering mechanism (i.e. atomic migration vs. particle migration) either from particle size distributions of sintered particles or from fitting of kinetic data with the simple power law equation. To elucidate the particle sintering mechanism, direct visualization at particle/atomic level under realistic conditions is necessary. For example, future advances in environmental TEM that allow experiments at true catalyst operation conditions could open the door in this direction. One limitation of this work is that particles smaller than 1 nanometer were not resolved by the used TEM instrument and are thus excluded from our analysis. As I show in paper IV, relevant and interesting redispersion processes may take place in this size regime.

Paper III

In Paper III, we further expand the applicability of the INPS platform by monitoring sintering of particles supported on a mesoporous support (instead of flat support as in the previous INPS studies^{197,201}), as typically used for example in the TWC. This is achieved by deposition of thin films of porous alumina on INPS sensor chips, followed by Pt wet-impregnation and calcination. A schematic illustration and representative SEM and STEM images of the Pt-impregnated porous alumina are shown in Figure 5.3. The images confirm the direct contact between the catalyst layer and the plasmonic gold nanodisks, as well as the homogeneous distribution of the Pt nanoparticles throughout the entire alumina matrix. The former is crucial since the sensing volume of the INPS chip only extends a few tens of nanometers from its surface.

To demonstrate the functionality of this new platform, real time sintering kinetics measurements of Pt particles on porous alumina at different temperatures and in different oxygen concentrations are carried out. Specifically, the samples are exposed to 4 % O₂ diluted in Ar for 10 hours at different temperatures (550-625 °C). Figure 5.3 shows the time evolution of the plasmonic peak shift ($\Delta\lambda$) during this treatment. We observe a red-shift with a magnitude that scales with the sintering temperature, indicating more severe sintering at higher temperatures. This is in agreement with the known temperature-dependence of nanoparticle sintering processes.

In conclusion, this study extends the applicability of in operando nanoplasmonic spectroscopy in catalysis by bridging the structure gap and making measurements on realistic porous three-dimensional catalyst systems possible. This opens new opportunities to apply this experimental methodology in catalysis research. Nevertheless, it should also be noted that the extent of

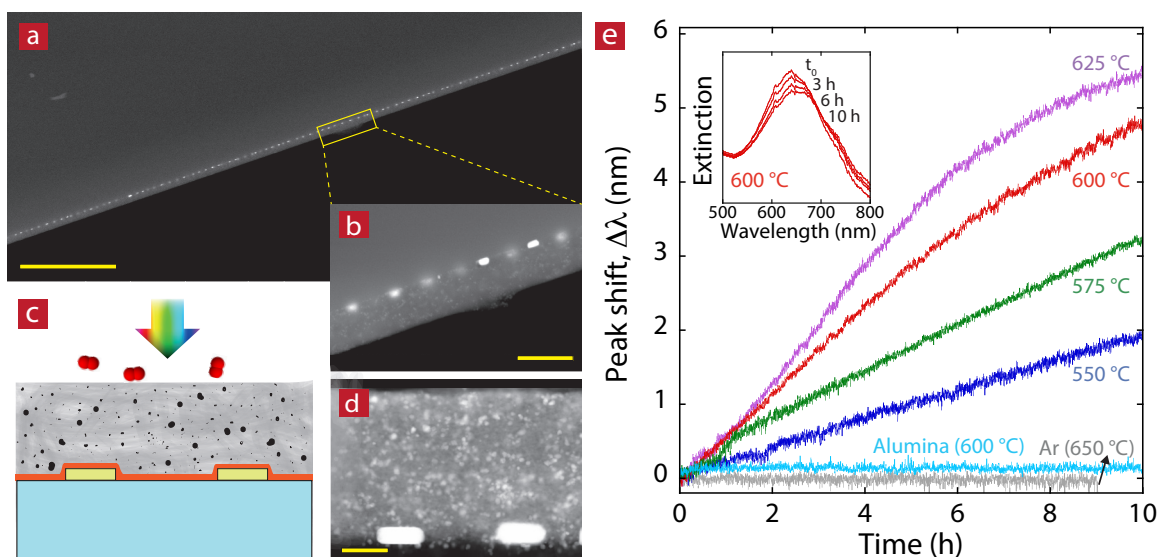


Figure 5.3. (a, b) Cross-sectional SEM images of the sensor chip with the catalyst system on top. The micrographs confirm a uniform mesoporous alumina washcoat layer with a thickness of around 400 nm. Scale bar in panel a: 5 μm , b: 500 nm. (c) Schematics of the in operando plasmonic spectroscopy of oxygen-induced sintering of the Pt nanoparticles in the washcoat. (d) STEM image of a cross section through the entire arrangement, revealing that the impregnated Pt particles are homogeneously dispersed within the alumina support. Scale bar: 100 nm. (e) Real time INPS sintering kinetics of Pt particles supported on a mesoporous alumina washcoat, measured at 550, 575, 600 and 625 $^{\circ}\text{C}$ in 4 % O_2 in Ar. The plot includes also two control experiments showing (i) the stability of the bare γ -alumina layer (i.e. without Pt nanoparticles – light blue curve), and (ii) that a sample impregnated with Pt exhibits a stable signal during the exposure to pure Ar at 650 $^{\circ}\text{C}$, when no sintering is expected to occur (grey curve). The inset shows a selection of raw extinction spectra along the timeline of a sintering experiment for the 600 $^{\circ}\text{C}$ sample.

sintering measured by INPS can be compared solely on a qualitative basis as long as no direct correlation between the INPS signal shift and a particle descriptor like the mean diameter is established experimentally, as shown on Paper I.

Paper IV

The importance and role of support heterogeneity in sintering was highlighted in Paper II. However, due to the nature of the support material, a clear experimental identification of the support heterogeneity is lacking in that study. Thus, in Paper IV, to mimic the heterogeneous surface of mesoporous supports, we use nanolithography to introduce controlled three-dimensional structural heterogeneity. Specifically, arrays of alumina nanocones with flat surfaces between them are fabricated on TEM membranes. Pt particles are then grown all over the support by e-beam evaporation. Interestingly, the

average size of formed nanoparticles on the cones is lower compared to the particles on the flat surfaces (Figure 5.4 a,b). The most plausible reason for the observed difference in the initial particle size distribution is a higher defect density on the cones (acting as nucleation sites) compared to the flat regions. In fact, side-view imaging of the cones reveals structural irregularities over the cone walls. Thus, we achieve a platform consisting of two types of surfaces that differ in terms of defect density, as well as initial particle size distribution. The new platform is used together with aberration-corrected HAADF-STEM to investigate the evolution of the Pt particle size distribution on the cones and the flat regions during exposure to 4 % O₂ diluted in Ar at 600 °C (Figure 5.4 c).

Intriguingly, while the particles on the cones are rapidly completely redispersed into particles of the order of 1 nm, both shrinkage and growth (including also some redispersion) can be observed on the flat surface, leading to a broader and bimodal size distribution. The observed initial rapid shrinkage on the cones can be explained by the gradient in the initial Pt particle size on the cones and flat surfaces, which favors the diffusion of monomers from particles on the cones (that are smaller on average) to the flat surface. Simultaneously, as a consequence of the redispersion, the particle density also significantly increases on the cones during the first 10 minutes of aging. The proposed reason for these observations is that abundant structural defect sites (“steps”) on the cones act as anchoring sites for the diffusing monomers, which leads to the observed redispersion. Surprisingly, the formed small particles are very stable even after 60 minutes of aging, indicating a stabilizing effect of the defect sites. These processes are amplified and efficiently visualized by the used nanostructured surface due to (i) higher support defect density on the nanocones compared to the flat surfaces in between, and (ii) initially different Pt particle size distributions on the cones and on the flat surfaces. Hence, the nanostructured surface facilitates the clear identification of catalyst redispersion in oxidizing conditions, and experimentally identifies a mechanism that gives rise to (transient) bi- or multimodal particle size distributions during sintering. The results also potentially pave the way to rational design of supported catalysts with higher stability, as well as to strategies towards catalyst redispersion in oxidizing conditions.

At the same time, when critically assessing this work, it is worth mentioning that post mortem TEM imaging of similar (but not identical) samples, as we have done, might lead to the following complications; first, there might be inhomogeneity within different samples (although Pt particles were grown on all the samples at the same time) and the aging conditions, which can cause error in PSD analysis. Secondly, events that occur between the designated aging

intervals might be missed. For example, unlike our observation, it is not unreasonable to expect that the particles on the flat surface that are located closest to the cone walls become larger compared to the particles further away. This is due to the higher probability of attachment of monomers that diffuse from the cones to the flat areas.

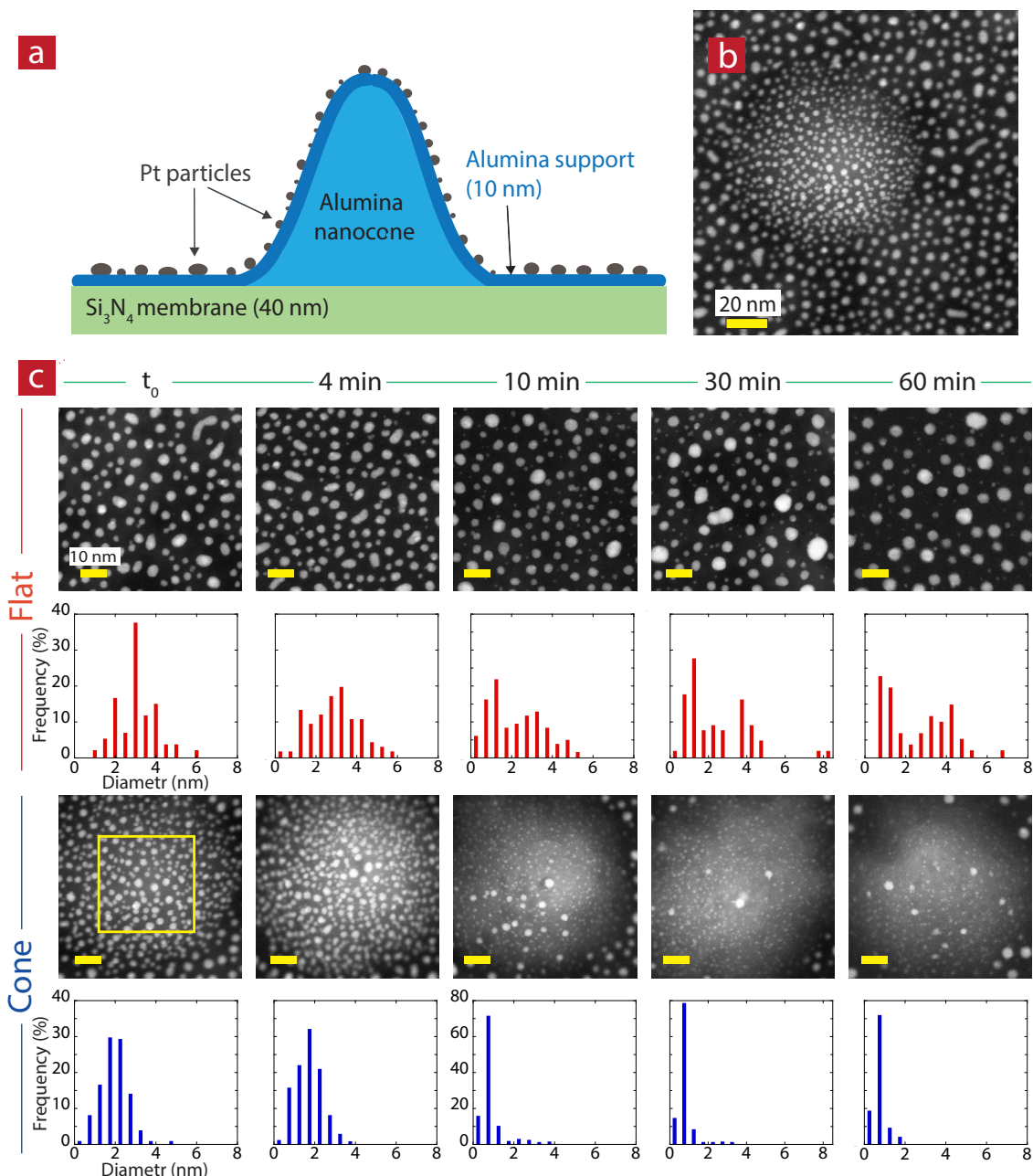


Figure 5.4. (a) Schematic illustration of Pt nanoparticles supported on a nanostructured alumina surface on a TEM membrane. (b) Scanning transmission electron microscopy (STEM) image of a single nanocone and the adjacent flat area decorated with Pt nanoparticles. Note the clear difference in Pt particle size and density on the cone and on the flat area. (c) STEM images and corresponding size distributions of alumina-supported Pt particles during sintering in 4% O₂ at 600 °C on both flat areas and fabricated nanocones (scale bare: 10 nm). The yellow square represents the area on each cone that is analyzed to obtain the size distributions.

Conclusions and Outlook

Over the years, numerous theoretical and experimental studies have been performed to better understand the complexity of supported nanoparticle sintering. They all have common goals, namely, to understand how to minimize/prevent the particle sintering at different conditions and/or find strategies to redisperse the sintered particles. In line with these ambitions, this thesis explores the adsorbate-induced sintering of Pt nanoparticles on silica and alumina supports of different kind under realistic conditions in terms of pressure and temperature by applying both newly developed and established experimental techniques. It therefore also constitutes an attempt to bridge the pressure and structure gaps in catalysis science.

Specifically, as one track of my work, I addressed the need for operando tools for the scrutiny of sintering kinetics by demonstrating the applicability and flexibility of INPS as operando tool to measure Pt sintering kinetics on different support materials and in different gas environments (Paper I). Furthermore, to bridge the structure gap, we showed the ability of INPS to monitor sintering of Pt nanoparticles dispersed on a mesoporous γ -alumina washcoat layer in operando (Paper III). As the main conclusion, the obtained results demonstrate that the INPS kinetic data is very suitable for screening of nanoparticle sintering at varying conditions (e.g. temperature and gas type/concentration). Thus, it can provide important clues on the role of different parameters and it can efficiently help identifying the conditions at which sintering is less severe. Consequently, INPS data obtained in operando can serve as a guideline for further and more detailed and specialized experiments, e.g. microscopy or other types of more advanced spectroscopy.

The second track of my thesis focused on elucidating the role of the support

material in coarsening of nanoparticles using (S)TEM. In Paper II, the evolution of Pt particle size distributions during sintering in O₂ as a function of time and temperature was analyzed, and the role of possible (however not experimentally identified) support heterogeneity as the reason for the made experimental observations was discussed theoretically. Our study thus highlights the importance of the support material when aiming at obtaining a complete picture of nanoparticle aging. At the same time, in our study we also cast doubt on deducing mechanisms based on either kinetics or particle size distributions alone, as commonly done in the literature. Our argumentation is mainly based on our observation of multimodal transient size distributions, which cannot efficiently be treated and taken into account when, for example, using the particle mean diameter as the sole descriptor of a sintering process. In Paper IV, we take the above one step further by introducing controlled structural heterogeneity (fabricated nanocones versus flat surface) on the model catalyst support, which results in significantly different Pt sintering/redispersion behavior compared to non-structured analogues. These observations give more insight into the origin of transient bi/multi-modal size distributions, and can potentially guide us to design routes that facilitate nanoparticle redispersion in oxidizing environments.

In the future, many avenues inspired by the work included in this thesis can be explored to further elucidate the sintering of catalyst nanoparticles under realistic conditions, and to further adapt the INPS platform to sintering studies. Some possible directions are summarized below.

(i) The details of the relationship between the INPS signal shift and the rearrangement of catalyst particles on the sensor chip surface are not yet well understood. Theoretical simulations of changes in Pt particles on individual sensor particles could help to clarify this relationship, which in turn, may help to better interpret the INPS data, and ideally made it possible to derive a universal relationship between INPS signal and the studied catalyst nanoparticle ensemble. One way to validate the simulation results is to exploit the INPS platform at the single gold particle level¹⁹⁵, in contrast to the present studies where arrays of gold sensor particles are used.

(ii) In order to gain information on the catalytic activity of supported nanoparticles while monitoring the sintering of particles, INPS can be complemented with mass spectrometry of reaction products. The INPS signal (extent of sintering) can then be directly correlated with catalyst activity. This type of experiment becomes particularly effective when using the porous catalyst on an INPS surface demonstrated in paper III, since it makes sure that

enough catalytic sites are available to guarantee strong mass spectrometry signal. A more ambitious outlook could be to combine INPS with other operando spectroscopic techniques such as EXAFS to acquire more information on, for example, the chemical state of particles/support during the sintering process.

(iii) Following up the work on nanostructuring of the support surface (Paper IV), one can imagine to further engineer the platform by altering the cone density, size and geometry (e.g. forming truncated cones by simply depositing less material). Moreover, it is possible to deposit nanoparticles of different types (e.g. Pd and Pt) or with different size distributions (instead of fabricating cones through the hole-mask). In this way, the heterogeneity in size distribution and type of nanoparticles – that occurs in technical catalysts – can be studied.

(iv) Regarding Paper IV, further and more direct mechanistic information about the sintering/redispersion processes we have observed occurring to different extents on the cone and the flat surfaces (or similar systems described above) can be obtained by using environmental/in situ (S)TEM. This technique can operate from the sub-10 mbar up to the atmospheric pressure regime when using special holders^{145,146}. In this way, direct continuous imaging of the evolution of particles on a specific sample region (e.g. consisting of different patches/particle size distributions) during sintering becomes possible at conditions – at least close to – application conditions.

Acknowledgments

This work was funded by and performed at the Competence Centre for Catalysis, which is hosted by Chalmers University of Technology, and financially supported by the Swedish Energy Agency, and the member companies: AB Volvo, ECAPS AB, Haldor Topsøe A/S, Scania CV AB, Volvo Car Corporation AB, and Wärtsilä Finland Oy.

The studied samples were fabricated at the MC2 nanofabrication laboratory at Chalmers University of Technology.

First of all, I would like to express my gratitude to my two main supervisors, **Christoph Langhammer** and **Henrik Grönbeck** for their remarkable supports that made it possible to accomplish this thesis.

Christoph Langhammer, I am truly grateful to have you as my supervisor, as I learned a lot from you through many constructive discussions and feedbacks. And thanks for being always available for helping me during this journey.

Henrik Grönbeck, your dedication to science has always been an inspiration for me. I appreciate all the time you put for me despite your busy schedule. I also greatly appreciate your effort on carefully reading this thesis, which made it much improved from its early stages.

I would also like to thank the following people:

Magnus Skoglundh, for giving me the opportunity to start my work at KCK, and all the helpful discussions on my project.

Igor Zorić, for being the one who first made me interested in the project (already in the interview), and also for reviewing parts of my thesis.

Vladimir Zhdanov, for all the fruitful discussions and collaboration on the paper II.

Eva Olsson, for the collaboration and discussions on Paper III and IV.

Tomasz Antosiewicz, for performing the FDTD simulations, and **Franceco Mazzotta**, for the additional experiments in Paper I.

Torben Pingel, for teaching me to operate Tecnai TEM, collaboration on Paper III and IV, and also all the fun time outside Chalmers.

All the former and current members of Chemical Physics for their support inside and outside the lab, especially the following people: **Elin Larsson**, for all the help with the lab works in the beginning of my project, **Carl**, for coaching me to operate the cleanroom tools, **Ferry**, for taking nice photos of my samples, **Farzin** for always sharing interesting ideas. **Anna**, for all the discussions and helps in the lab, and **Chris** for being a nice colleague and a flat mate!

My former and current office mates, **Kristina**, **Beniamino**, **Raja**, **Anna**, **Viktor**, **Adriana**, **Maxime**, **Mikael** and **Adam** for bringing a nice and friendly atmosphere to the workplace, and all the small and big helps.

Members of KCK, especially **Sheedeh** who helped me with catalyst synthesis.

Biological Physics group members who share the kitchen with us, and making a friendly working atmosphere. Special thanks to **Mokhtar** for always being a nice friend, and helping me with the idea of nanofabrication on thin membranes.

I owe my **family** a lot, for all their supports and encouragements during the past decades.

And last but not least, I would like to say a big thanks to **Anahid** for all the love, support, and friendship during these years.

Bibliography

- (1) Chorkendorff, I.; Niemantsverdriet, J. W. *Concepts of Modern Catalysis and Kinetics (2nd Ed.)*; Wiley-VCH, **2007**.
- (2) Rouquerol, J.; Avnir, D.; Fairbridge, C. W.; Everett, D. H.; Haynes, J. M.; Pernicone, N.; Ramsay, J. D. F.; Sing, K. S. W.; Unger, K. K. Recommendations for the Characterization of Porous Solids (Technical Report). *Pure Appl. Chem.* **1994**, *66*, 1739–1758.
- (3) Viñes, F.; Gomes, J. R. B.; Illas, F. Understanding the Reactivity of Metallic Nanoparticles: Beyond the Extended Surface Model for Catalysis. *Chem. Soc. Rev.* **2014**, *43*, 4922.
- (4) Valden, M. Onset of Catalytic Activity of Gold Clusters on Titania with the Appearance of Nonmetallic Properties. *Science* **1998**, *281*, 1647–1650.
- (5) Chen, M. S.; Goodman, D. W. The Structure of Catalytically Active Gold on Titania. *Science* **2004**, *306*, 252–255.
- (6) Mavrikakis, M.; Stoltze, P.; Nørskov, J. K. Making Gold Less Noble. *Catal. Letters* **2000**, *64*, 101–106.
- (7) Borg, H. J.; Reijerse, J. F. C.-J. M. C. -J. M.; van Santen, R. a.; Niemantsverdriet, J. W. The Dissociation Kinetics of NO on Rh(111) as Studied by Temperature Programmed Static Secondary Ion Mass Spectrometry and Desorption. *J. Chem. Phys.* **1994**, *101*, 10052–10063.
- (8) Hopstaken, M. J. P.; Niemantsverdriet, J. W. Lateral Interactions in the Dissociation Kinetics of NO on Rh(100). *J. Phys. Chem. B* **2000**, *104*, 3058–3066.
- (9) Uzio, D.; Berhault, G. Factors Governing the Catalytic Reactivity of Metallic Nanoparticles. *Catal. Rev.* **2010**, *52*, 106–131.

- (10) Roldán Cuenya, B. Metal Nanoparticle Catalysts Beginning to Shape-Up. *Acc. Chem. Res.* **2013**, *46*, 1682–1691.
- (11) Bell, A. T. The Impact of Nanoscience on Heterogeneous Catalysis. *Science* **2003**, *299*, 1688–1691.
- (12) IARC Working Group on the Evaluation of Carcinogenic Risks to humans. *Diesel and Gasoline Engine Exhausts and Some Nitroarenes*; International Agency for Research on Cancer (IARC), **2012**; Vol. 105.
- (13) Regulation (EC) No 715/2007 of the European Parliament and of the Council <http://eur-lex.europa.eu/LexUriServ/LexUriServ.do?uri=OJ:L:2007:171:0001:0016:EN:PDF>
- (14) Bartholomew, C. H. Mechanisms of Catalyst Deactivation. *Appl. Catal. A Gen.* **2001**, *212*, 17–60.
- (15) Saurat, M.; Bringezu, S. Platinum Group Metal Flows of Europe, Part 1. *J. Ind. Ecol.* **2008**, *12*, 754–767.
- (16) The components of autocatalyst demand http://www.platinum.matthey.com/media/1614393/the_components_of_autocatalyst_demand.pdf.
- (17) Cao, A.; Lu, R.; Vesper, G. Stabilizing Metal Nanoparticles for Heterogeneous Catalysis. *Phys. Chem. Chem. Phys.* **2010**, *12*, 13499–13510.
- (18) Johns, T. R.; Goeke, R. S.; Ashbacher, V.; Thüne, P. C.; Niemantsverdriet, J. W.; Kiefer, B.; Kim, C. H.; Balogh, M. P.; Datye, A. K. Relating Adatom Emission to Improved Durability of Pt-Pd Diesel Oxidation Catalysts. *J. Catal.* **2015**, *328*, 151–164.
- (19) Cao, A.; Vesper, G. G. Exceptional High-Temperature Stability through Distillation-like Self-Stabilization in Bimetallic Nanoparticles. *Nat Mater.* **2010**, *9*, 75–81.
- (20) Joo, S. H.; Park, J. Y.; Tsung, C.-K.; Yamada, Y.; Yang, P.; Somorjai, G. A. Thermally Stable Pt/mesoporous Silica Core-Shell Nanocatalysts for High-Temperature Reactions. *Nat. Mater.* **2009**, *8*, 126–131.
- (21) Argyle, M.; Bartholomew, C. Heterogeneous Catalyst Deactivation and Regeneration: A Review. *Catalysts* **2015**, *5*, 145–269.
- (22) Rodriguez, J. A.; Hrbek, J. Interaction of Sulfur with Well-Defined Metal and Oxide Surfaces: Unraveling the Mysteries behind Catalyst Poisoning and Desulfurization. *Acc. Chem. Res.* **1999**, *32*, 719–728.
- (23) Goodman, D. W. Chemical Modification of Chemisorptive and Catalytic Properties

of Nickel. *Appl. Surf. Sci.* **1984**, *19*, 1–13.

(24) Lang, N. D.; Holloway, S.; Nørskov, J. K. Electrostatic Adsorbate-Adsorbate Interactions: The Poisoning and Promotion of the Molecular Adsorption Reaction. *Surf. Sci.* **1985**, *150*, 24–38.

(25) Russell, A.; Epling, W. S. Diesel Oxidation Catalysts. *Catal. Rev.* **2011**, *53*, 337–423.

(26) Heck, R. M.; Farrauto, R. J.; Gulati, S. T. *Catalytic Air Pollution Control: Commercial Technology*; third.; John Wiley & Sons, 2009.

(27) Skoglundh, M.; Fridell, E. Strategies for Enhancing Low-Temperature Activity. *Top. Catal.* **2004**, *28*, 79–87.

(28) Gollob, R.; Dadyburjor, D. Regeneration of Model Supported Metal Catalysts. *J. Catal.* **1981**, *68*, 473–486.

(29) Le Normand, F.; Borgna, A.; Garetto, T. F.; Apesteguia, C. R.; Moraweck, B. Redispersion of Sintered Pt/Al₂O₃ Naphtha Reforming Catalysts: An in Situ Study Monitored by X-Ray Absorption Spectroscopy. *J. Phys. Chem.* **1996**, *100*, 9068–9076.

(30) Galisteo, F. C.; Mariscal, R.; Granados, M. L.; Fierro, J. L. G.; Daley, R. A.; Anderson, J. A. Reactivation of Sintered Pt/Al₂O₃ Oxidation Catalysts. *Appl. Catal. B Environ.* **2005**, *59*, 227–233.

(31) Nagai, Y.; Dohmae, K.; Ikeda, Y.; Takagi, N.; Tanabe, T.; Hara, N.; Guilera, G.; Pascarelli, S.; Newton, M. A.; Kuno, O.; *et al.* In Situ Redispersion of Platinum Autoexhaust Catalysts: An on-Line Approach to Increasing Catalyst Lifetimes? *Angew. Chem. Int. Ed. Engl.* **2008**, *47*, 9303–9306.

(32) Smoluchowski, M. von. Drei Vorträge Über Diffusion, Brownsche Bewegung Und Koagulation von Kolloidteilchen. *Zeitschrift für Phys.* **1916**, *17*, 557–585.

(33) Wynblatt, P.; Gjostein, N. A. Supported Metal Crystallites. *Prog. Solid State Chem.* **1975**, *9*, 21–58.

(34) Ertl, G. Wilhelm Ostwald: Founder of Physical Chemistry and Nobel Laureate 1909. *Angew. Chem. Int. Ed. Engl.* **2009**, *48*, 6600–6606.

(35) Hansen, T. W.; Delariva, A. T.; Challa, S. R.; Datye, A. K. Sintering of Catalytic Nanoparticles: Particle Migration or Ostwald Ripening? *Acc. Chem. Res.* **2013**, *46*, 1720–1730.

(36) Fukamori, Y.; König, M.; Yoon, B.; Wang, B.; Esch, F.; Heiz, U.; Landman, U.

Fundamental Insight into the Substrate-Dependent Ripening of Monodisperse Clusters. *ChemCatChem* **2013**, *5*, 3330–3341.

(37) Sehested, J. Sintering of Nickel Steam-Reforming Catalysts. *J. Catal.* **2003**, *217*, 417–426.

(38) Campbell, C. T.; Parker, S. C.; Starr, D. E. The Effect of Size-Dependent Nanoparticle Energetics on Catalyst Sintering. *Science* **2002**, *298*, 811–814.

(39) Bartholomew, C. H. Mechanisms of Catalyst Deactivation. *Appl. Catal. A Gen.* **2001**, *212*, 17–60.

(40) Sault, A.; Tikare, V. A New Monte Carlo Model for Supported-Catalyst Sintering. *J. Catal.* **2002**, *211*, 19–32.

(41) Kovalyov, E. V.; Elokhin, V. I. Simulation of Adsorption Processes Performance over Supported Metal Nanoparticles. *Chem. Eng. J.* **2009**, *154*, 88–93.

(42) Prévot, G. Ostwald Ripening of Three-Dimensional Clusters on a Surface Studied with an Ultrafast Kinetic Monte Carlo Algorithm. *Phys. Rev. B* **2011**, *84*, 1–9.

(43) Zhdanov, V. P. Kinetics of Migration and Coalescence of Supported Nm-Sized Metal Particles. *Surf. Rev. Lett.* **2008**, *15*, 217–220.

(44) Ruckenstein, E.; Pulvermacher, B. Kinetics of Crystallite Sintering during Heat Treatment of Supported Metal Catalysts. *AIChE J.* **1973**, *19*, 356–364.

(45) Parker, S.; Campbell, C. Kinetic Model for Sintering of Supported Metal Particles with Improved Size-Dependent Energetics and Applications to Au on TiO₂(110). *Phys. Rev. B* **2007**, *75*, 1–15.

(46) Houk, L. R.; Challa, S. R.; Grayson, B.; Fanson, P.; Datsy, A. K. The Definition of “Critical Radius” for a Collection of Nanoparticles Undergoing Ostwald Ripening. *Langmuir* **2009**, *25*, 11225–11227.

(47) Wynblatt, P.; Gjosteis, N. A. Particle Growth in Model Supported Metal Catalysts-I. Theory. *Acta Metall.* **1976**, *24*, 1165–1174.

(48) Fuentes, G. A.; Gamas, E. D. Towards A Better Understanding of Sintering Phenomena in Catalysis. In *Catalyst Deactivation; Proceedings of the 5th International Symposium*; Catalysis, Elsevier; **1991**, *68*, 637–644.

(49) Bartholomew, C. H. Sintering Kinetics of Supported Metals: New Perspectives from a Unifying GPLE Treatment. *Appl. Catal. A Gen.* **1993**, *107*, 1–57.

- (50) Wettergren, K.; Schweinberger, F. F.; Deiana, D.; Ridge, C. J.; Crampton, A. S.; Ro, M. D.; Hansen, T. W.; Zhdanov, V. P.; Heiz, U.; Langhammer, C. High Sintering Resistance of Size-Selected Platinum Cluster Catalysts by Suppressed Ostwald Ripening. *Nano Lett.* **2014**, *14*, 5803–5809.
- (51) Lifshitz, I. M.; Slyozov, V. V. The Kinetics of Precipitation from Supersaturated Solid Solutions. *J. Phys. Chem. Solids* **1961**, *19*, 35–50.
- (52) Wagner, C. Theorie Der Alterung von Niederschlägen Durch Umlösen (Ostwald-Reifung). *Zeitschrift für Elektrochemie, Berichte der Bunsengesellschaft für Phys. Chemie* **1961**, *65*, 581–591.
- (53) Chakraverty, B. K. Grain Size Distribution in Thin films—1. Conservative Systems. *J. Phys. Chem. Solids* **1967**, *28*, 2401–2412.
- (54) Ouyang, R.; Liu, J.-X.; Li, W.-X. Atomistic Theory of Ostwald Ripening and Disintegration of Supported Metal Particles under Reaction Conditions. *J. Am. Chem. Soc.* **2013**, *135*, 1760–1771.
- (55) Goldsmith, B. R.; Sanderson, E. D.; Ouyang, R.; Li, W.-X. CO- and NO-Induced Disintegration and Redispersion of Three-Way Catalysts Rhodium, Palladium, and Platinum: An Ab Initio Thermodynamics Study. *J. Phys. Chem. C* **2014**, *118*, 9588–9597.
- (56) Gruber, E. E. Calculated Size Distributions for Gas Bubble Migration and Coalescence in Solids. *J. Appl. Phys.* **1967**, *38*, 243.
- (57) Willertz, L. E.; Shewmon, P. G.; Electric, W.; Lab-, A. N. Diffusion of Helium Gas Bubbles in Gold and Copper Foils. **1970**, *1*, 2217.
- (58) Pulvermacher, B.; Ruckenstein, E. Growth Kinetics and the Size Metal Distributions of Supported Metal Crystallites. *J. Catal.* **1973**, *29*, 224–245.
- (59) Granqvist, C. G.; Buhrman, R. A. Ultrafine Metal Particles. *J. Appl. Phys.* **1976**, *47*, 2200.
- (60) Hansen, T. W. Sintering and Particle Dynamics in Supported Metal Catalysts, *PhD Thesis*, Technical University of Denmark, **2006**.
- (61) Zinke-Allmang, M.; Feldman, L. C.; Nakahara, S.; Davidson, B. A. Growth Mechanism and Clustering Phenomena: The Ge-on-Si System. *Phys. Rev. B* **1989**, *39*, 7848–7851.
- (62) Rosenfeld, G.; Morgenstern, K.; Esser, M.; Comsa, G. Dynamics and Stability of Nanostructures on Metal Surfaces. *Appl. Phys. A Mater. Sci. Process.* **1999**, *69*, 489–496.

- (63) Datye, A. K.; Xu, Q.; Kharas, K. C.; McCarty, J. M. Particle Size Distributions in Heterogeneous Catalysts: What Do They Tell Us about the Sintering Mechanism? *Catal. Today* **2006**, *111*, 59–67.
- (64) Wanke, S. E. Comments on the Sintering Mechanism of Supported Metal Catalysts. *J. Catal.* **1977**, *46*, 234–237.
- (65) DeLaRiva, A. T.; Hansen, T. W.; Challa, S. R.; Datye, A. K. In Situ Transmission Electron Microscopy of Catalyst Sintering. *J. Catal.* **2013**, *308*, 291–305.
- (66) Parkinson, G. S.; Novotny, Z.; Argentero, G.; Schmid, M.; Pavelec, J.; Kosak, R.; Blaha, P.; Diebold, U. Carbon Monoxide-Induced Adatom Sintering in a Pd-Fe₃O₄ Model Catalyst. *Nat. Mater.* **2013**, *12*, 724–728.
- (67) Fiedorow, R. M. J.; Chahar, B. S.; Wanke, S. E. The Sintering of Supported Metal Catalysts II. Comparison of Sintering Rates of Supported Pt, Ir, and Rh Catalysts in Hydrogen and Oxygen. *J. Catal.* **1978**, *51*, 193–202.
- (68) Hu, K.-J.; Plant, S. R.; Ellis, P. R.; Brown, C. M.; Bishop, P. T.; Palmer, R. E. Atomic Resolution Observation of a Size-Dependent Change in the Ripening Modes of Mass-Selected Au Nanoclusters Involved in CO Oxidation. *J. Am. Chem. Soc.* **2015**, *137*, 15161–15168.
- (69) Simonsen, S. B.; Chorkendorff, I.; Dahl, S.; Skoglundh, M.; Meinander, K.; Jensen, T. N.; Lauritsen, J. V.; Helveg, S. Effect of Particle Morphology on the Ripening of Supported Pt Nanoparticles. *J. Phys. Chem. C* **2012**, *116*, 5646–5653.
- (70) Ono, L.; Sudfeld, D.; Roldán Cuenya, B. In Situ Gas-Phase Catalytic Properties of TiC-Supported Size-Selected Gold Nanoparticles Synthesized by Diblock Copolymer Encapsulation. *Surf. Sci.* **2006**, *600*, 5041–5050.
- (71) Ono, L. K.; Roldán Cuenya, B. Effect of Interparticle Interaction on the Low Temperature Oxidation of CO over Size-Selected Au Nanocatalysts Supported on Ultrathin TiC Films. *Catal. Letters* **2007**, *113*, 86–94.
- (72) Thessing, J.; Qian, J.; Chen, H.; Pradhan, N.; Peng, X. Interparticle Influence on Size/size Distribution Evolution of Nanocrystals. *J. Am. Chem. Soc.* **2007**, *129*, 2736–2737.
- (73) Matos, J.; Ono, L. K.; Behafarid, F.; Croy, J. R.; Mostafa, S.; DeLaRiva, A. T.; Datye, A. K.; Frenkel, A. I.; Roldán Cuenya, B. In Situ Coarsening Study of Inverse Micelle-Prepared Pt Nanoparticles Supported on γ -Al₂O₃: Pretreatment and Environmental Effects. *Phys. Chem. Chem. Phys.* **2012**, *14*, 11457–11467.
- (74) Chen, M.; Schmidt, L. D. Morphology and Sintering of Pt Crystallites on Amorphous

SiO₂, *J. Catal.* **1978**, *55*, 348–360.

(75) Wanke, S. Sintering of Commercial Supported Platinum Group Metal Catalysts. In *Progress in Catalyst Deactivation SE - 14*; Figueiredo, J., Ed.; NATO Advanced Study Institutes Series; Springer Netherlands, **1982**, *54*, 315–328.

(76) Lee, T.; Kim, Y. G. Redispersions of Supported Platinum Catalysts. *J. Catal.* **1984**, *90*, 279–291.

(77) Simonsen, S. B. Sintering of Oxide-Supported Pt and Pd Nanoparticles in Air Studied by in Situ TEM, *PhD Thesis*, Technical University of Denmark, **2011**.

(78a) Morgenstern, K.; Rosenfeld, G.; Comsa, G. Local Correlation during Ostwald Ripening of Two-Dimensional Islands on Ag(111). *Surf. Sci.* **1999**, *441*, 289–300.

(78b) Wen, J.-M.; Evans, J. W.; Bartelt, M. C.; Burnett, J. W.; Thiel, P. A. Coarsening Mechanisms in a Metal Film: From Cluster Diffusion to Vacancy Ripening. *Phys. Rev. Lett.* **1996**, *76*, 652–655.

(79) Wallace, W. T.; Min, B. K.; Goodman, D. W. The Stabilization of Supported Gold Clusters by Surface Defects. *J. Mol. Catal. A Chem.* **2005**, *228*, 3–10.

(80) Behafarid, F.; Roldán-Cuenya, B. Surface Science Coarsening Phenomena of Metal Nanoparticles and the Influence of the Support Pre-Treatment: Pt/TiO₂(110). *Surf. Sci.* **2012**, *606*, 908–918.

(81) Rieboldt, F.; Helveg, S.; Bechstein, R.; Lammich, L.; Besenbacher, F.; Lauritsen, J. V.; Wendt, S. Formation and Sintering of Pt Nanoparticles on Vicinal Rutile TiO₂ Surfaces. *Phys. Chem. Chem. Phys.* **2014**, *16*, 21289–21299.

(82) Ahn, T. M.; Tien, J. K.; Wynblatt, P. Coarsening Kinetics of Platinum Particles on Curved Oxide Substrates. *J. Catal.* **1980**, *66*, 335–346.

(83) Campbell, C. T.; Sellers, J. R. V. Anchored Metal Nanoparticles: Effects of Support and Size on Their Energy, Sintering Resistance and Reactivity. *Faraday Discuss.* **2013**, *162*, 9.

(84) Campbell, C. T. The Energetics of Supported Metal Nanoparticles: Relationships to Sintering Rates and Catalytic Activity. *Acc. Chem. Res.* **2013**, *46*, 1712–1719.

(85) Jensen, M. C. R.; Venkataramani, K.; Helveg, S.; Clausen, B. S.; Reichling, M.; Besenbacher, F.; Lauritsen, J. V. Morphology, Dispersion, and Stability of Cu Nanoclusters on Clean and Hydroxylated α -Al₂O₃(0001) Substrates. *J. Phys. Chem. C* **2008**, *112*, 16953–16960.

- (86) Brown, M. A; Carrasco, E.; Sterrer, M.; Freund, H.-J. Enhanced Stability of Gold Clusters Supported on Hydroxylated MgO(001) Surfaces. *J. Am. Chem. Soc.* **2010**, *132*, 4064–4065.
- (87) Addou, R.; Senftle, T. P.; O'Connor, N.; Janik, M. J.; van Duin, A. C. T.; Batzill, M. Influence of Hydroxyls on Pd Atom Mobility and Clustering on Rutile TiO₂(011)-2×1. *ACS Nano* **2014**, *2*.
- (88) Kalakkad, D.; Datye, A. K.; Robota, H. Interaction of Platinum and Ceria Probed by Transmission Electron Microscopy and Catalytic Reactivity. *Appl. Catal. B Environ.* **1992**, *1*, 191–219.
- (89) Kundakovic, L.; Flytzani-Stephanopoulos, M. Cu- and Ag-Modified Cerium Oxide Catalysts for Methane Oxidation. *J. Catal.* **1998**, *179*, 203–221.
- (90) Shinjoh, H.; Hatanaka, M.; Nagai, Y.; Tanabe, T.; Takahashi, N.; Yoshida, T.; Miyake, Y. Suppression of Noble Metal Sintering Based on the Support Anchoring Effect and Its Application in Automotive Three-Way Catalysis. *Top. Catal.* **2009**, *52*, 1967–1971.
- (91) Farmer, J. A; Campbell, C. T. Ceria Maintains Smaller Metal Catalyst Particles by Strong Metal-Support Bonding. *Science* **2010**, *329*, 933–936.
- (92) Fiedorow, R.; Wanke, S. The Sintering of Supported Metal catalystsI. Redispersions of Supported Platinum in Oxygen. *J. Catal.* **1976**, *43*, 34–42.
- (93) Rubel, M.; Pszonicka, M.; Ebel, M. F.; Jabłoński, A.; Palczewska, W. Oxygen Generated Platinum, Rhodium and Palladium Volatile Losses from Pure Metals and Their Alloys. *J. Less Common Met.* **1986**, *125*, 7–24.
- (94) Lamber, R.; Romanowski, W. Dispersion Changes of Platinum Supported on Silica Glass during Thermal Treatment in Oxygen and Hydrogen Atmospheres. *J. Catal.* **1987**, *105*, 213–226.
- (95) Horch, S.; Lorensen, H. T.; Helveg, S.; Laegsgaard, E.; Stensgaard, I.; Jacobsen, K. W.; Norskov, J. K.; Besenbacher, F. Enhancement of Surface Self-Diffusion of Platinum Atoms by Adsorbed Hydrogen. **1999**, *398*, 99–101.
- (96) Ling, W.; Bartelt, N.; Pohl, K.; de la Figuera, J.; Hwang, R.; McCarty, K. Enhanced Self-Diffusion on Cu(111) by Trace Amounts of S: Chemical-Reaction-Limited Kinetics. *Phys. Rev. Lett.* **2004**, *93*, 166101.
- (97) Baker, R. Effect of Wetting on the Morphology of Supported Platinum Crystallites. *J. Catal.* **1980**, *63*, 523–525.

- (98) Harris, P. J. F. Sulphur-Induced Faceting of Platinum Catalyst Particles. *Nature* **1986**, *323*, 792–794.
- (99) Hansen, P. L.; Wagner, J. B.; Helveg, S.; Rostrup-Nielsen, J. R.; Clausen, B. S.; Topsøe, H. Atom-Resolved Imaging of Dynamic Shape Changes in Supported Copper Nanocrystals. *Science* **2002**, *295*, 2053–2055.
- (100) Newton, M. a; Belver-Coldeira, C.; Martínez-Arias, A.; Fernández-García, M. Dynamic in Situ Observation of Rapid Size and Shape Change of Supported Pd Nanoparticles during CO/NO Cycling. *Nat. Mater.* **2007**, *6*, 528–532.
- (101) Crozier, P. a; Wang, R.; Sharma, R. In Situ Environmental TEM Studies of Dynamic Changes in Cerium-Based Oxides Nanoparticles during Redox Processes. *Ultramicroscopy* **2008**, *108*, 1432–1440.
- (102) Nolte, P.; Stierle, A.; Jin-Phillipp, N. Y.; Kasper, N.; Schulli, T. U.; Dosch, H. Shape Changes of Supported Rh Nanoparticles During Oxidation and Reduction Cycles. *Science* **2008**, *321*, 1654–1658.
- (103) Yoshida, H.; Kuwauchi, Y.; Jinschek, J. R.; Sun, K.; Tanaka, S.; Kohyama, M.; Shimada, S.; Haruta, M.; Takeda, S. Visualizing Gas Molecules Interacting with Supported Nanoparticulate Catalysts at Reaction Conditions. *Science* **2012**, *335*, 317–319.
- (104) Vendelbo, S. B.; Elkjær, C. F.; Falsig, H.; Puspitasari, I.; Dona, P.; Mele, L.; Morana, B.; Nelissen, B. J.; van Rijn, R.; Creemer, J. F.; *et al.* Visualization of Oscillatory Behaviour of Pt Nanoparticles Catalysing CO Oxidation. *Nat. Mater.* **2014**, 1–48.
- (105) Porsgaard, S.; Merte, L. R.; Ono, L. K.; Behafarid, F.; Matos, J.; Helveg, S.; Salmeron, M.; Roldán-Cuenya, B.; Besenbacher, F. Stability of Platinum Nanoparticles Supported on SiO₂/Si(111): A High-Pressure X-Ray Photoelectron Spectroscopy Study. *ACS Nano* **2012**, *6*, 10743–10749.
- (106) Behafarid, F.; Roldán-Cuenya, B. Towards the Understanding of Sintering Phenomena at the Nanoscale: Geometric and Environmental Effects. *Top. Catal.* **2013**, *56*, 1542–1559.
- (107) Ruckenstein, E.; Malhotra, M. L. Splitting of Platinum Crystallites Supported on Thin, Nonporous Alumina Films. *J. Catal.* **1976**, *41*, 303–311.
- (108) Ruckenstein, E.; Chu, Y. Redispersion of Platinum Crystallites Supported on alumina—Role of Wetting. *J. Catal.* **1979**, *59*, 109–122.

- (109) Stulga, J. .; Wynblatt, P.; Tien, J. K. Particle Splitting and Redispersion Phenomena in Model Alumina-Supported Platinum Catalysts. *J. Catal.* **1980**, *62*, 59–69.
- (110) Sushumna, I.; Ruckenstein, E. Redispersion of Pt/alumina via Film Formation. *J. Catal.* **1987**, *108*, 77–96.
- (111) Rickard, J.; Genovese, L.; Moata, A.; Nitsche, S. Redispersion of Platinum on Pt/Al₂O₃ Model Catalyst in Oxygen Studied by Transmission Electron Microscopy. *J. Catal.* **1990**, *121*, 141–152.
- (112) Johnson, M. F. L.; Keith, C. D. The State Of Platinum In Re-Forming Catalysts. *J. Phys. Chem.* **1963**, *67*, 200–201.
- (113) Weller, S. W.; Montagna, A. A. O₂ Chemisorption at High Temperatures on Platinum-Alumina and Platinum-Zeolite. *J. Catal.* **1971**, *20*, 394–407.
- (114) Straguzzi, G.; Aduriz, H. R.; Gigola, E. Redispersion of Platinum on Alumina Support. *J. Catal.* **1980**, *66*, 171–183.
- (115) Lee, T.; Kim, Y. G. Dispersion of Supported Platinum Catalysts in Oxygen I. Experimental Evidences of Redispersion. *Korean J. Chem. Eng.* **1985**, *2*, 55–61.
- (116) Simonsen, S. B.; Chorkendorff, I.; Dahl, S.; Skoglundh, M.; Sehested, J.; Helveg, S. Direct Observations of Oxygen-Induced Platinum Nanoparticle Ripening Studied by in Situ TEM. *J. Am. Chem. Soc.* **2010**, *132*, 7968–7975.
- (117) Löf, P.; Stenbom, B.; Norden, H.; Kasemo, B. Rapid Sintering in NO of Nanometer-Sized Pt Particles on γ -Al₂O₃ Observed by CO Temperature-Programmed Desorption and Transmission Electron Microscopy. *J. Catal.* **1993**, *144*, 60–76.
- (118) Chu, Y.; Ruckenstein, E. On the Sintering of Platinum on Alumina Model Catalyst. *J. Catal.* **1978**, *55*, 281–298.
- (119) Graham, A. G.; Wanke, S. E. The Sintering of Supported Metal Catalysts III. The Thermal Stability of Bimetallic Pt-Ir Catalysts Supported on Alumina. *J. Catal.* **1981**, *68*, 1–8.
- (120) Alexeev, O.; Kim, D.-W.; Graham, G. W.; Shelef, M.; Gates, B. C. Temperature-Programmed Desorption of Hydrogen from Platinum Particles on γ -Al₂O₃: Evidence of Platinum-Catalyzed Dehydroxylation of γ -Al₂O₃. *J. Catal.* **1999**, *185*, 170–181.
- (121) Simonsen, S. B.; Chorkendorff, I.; Dahl, S.; Skoglundh, M.; Sehested, J.; Helveg, S. Ostwald Ripening in a Pt/SiO₂ Model Catalyst Studied by in Situ TEM. *J. Catal.* **2011**, *281*, 147–155.

- (122) Chusuei, C. C.; Lai, X.; Luo, K.; Goodman, D. W. Modeling Heterogeneous Catalysts : Metal Clusters on Planar Oxide Supports. *Top. Catal.* **2001**, *14*, 71–83.
- (123) Tao, F. F.; Salmeron, M. In Situ Studies of Chemistry and Structure of Materials in Reactive Environments. *Science* **2011**, *331*, 171–174.
- (124) Frenkel, A. I.; Rodriguez, J. A.; Chen, J. G. Synchrotron Techniques for In Situ Catalytic Studies: Capabilities, Challenges, and Opportunities. *ACS Catal.* **2012**, *2*, 2269–2280.
- (125) Zhang, S.; Nguyen, L.; Zhu, Y.; Zhan, S.; Tsung, C.-K. F.; Tao, F. F. In-Situ Studies of Nanocatalysis. *Acc. Chem. Res.* **2013**, *46*, 1731–1739.
- (126) Park, J. Y. *Current Trends of Surface Science and Catalysis*; Park, J. Y., Ed.; Springer New York: New York, NY, **2014**.
- (127) Su, D. S.; Zhang, B.; Schlögl, R. Electron Microscopy of Solid Catalysts—Transforming from a Challenge to a Toolbox. *Chem. Rev.* **2015**, *115*, 2818–2882.
- (128) Friedrich, H.; de Jongh, P. E.; Verkleij, A. J.; de Jong, K. P. Electron Tomography for Heterogeneous Catalysts and Related Nanostructured Materials. *Chem. Rev.* **2009**, *109*, 1613–1629.
- (129) Prieto, G.; Zecevic, J.; Friedrich, H.; de Jong, K. P.; de Jongh, P. E. Towards Stable Catalysts by Controlling Collective Properties of Supported Metal Nanoparticles. *Nat. Mater.* **2013**, *12*, 34–39.
- (130) Mostafa, S.; Behafarid, F.; Croy, J. R.; Ono, L. K.; Li, L.; Yang, J. C.; Frenkel, A. I.; Roldán Cuenya, B. Shape-Dependent Catalytic Properties of Pt Nanoparticles. *J. Am. Chem. Soc.* **2010**, *132*, 15714–15719.
- (131) Roldán Cuenya, B.; Croy, J. R.; Mostafa, S.; Behafarid, F.; Li, L.; Zhang, Z.; Yang, J. C.; Wang, Q.; Frenkel, A. I. Solving the Structure of Size-Selected Pt Nanocatalysts Synthesized by Inverse Micelle Encapsulation. *J. Am. Chem. Soc.* **2010**, *132*, 8747–8756.
- (132) Carlsson, A.; Puig-Molina, A.; Janssens, T. V. W. New Method for Analysis of Nanoparticle Geometry in Supported Fcc Metal Catalysts with Scanning Transmission Electron Microscopy. *J. Phys. Chem. B* **2006**, *110*, 5286–5293.
- (133) Li, Z. Y.; Young, N. P.; Di Vece, M.; Palomba, S.; Palmer, R. E.; Bleloch, A. L.; Curley, B. C.; Johnston, R. L.; Jiang, J.; Yuan, J. Three-Dimensional Atomic-Scale Structure of Size-Selected Gold Nanoclusters. *Nature* **2008**, *451*, 46–48.
- (134) Giorgio, S.; Cabié, M.; Henry, C. R. Dynamic Observations of Au Catalysts by

Environmental Electron Microscopy. *Gold Bull.* **2008**, *41*, 167–173.

(135) Hansen, T. W.; Wagner, J. B. Catalysts under Controlled Atmospheres in the Transmission Electron Microscope. *ACS Catal.* **2014**, *4*, 1673–1685.

(136) *Controlled Atmosphere Electron Microscopy*; Hansen, T. W.; Wagner, J. B., Eds.; Springer International Publishing Switzerland, **2016**.

(137) Baker, R. T. K. In Situ Electron Microscopy Studies of Catalyst Particle Behavior. *Catal. Rev.* **1979**, *19*, 161–209.

(138) Asoro, M. A.; Kovar, D.; Shao-Horn, Y.; Allard, L. F.; Ferreira, P. J. Coalescence and Sintering of Pt Nanoparticles: In Situ Observation by Aberration-Corrected HAADF STEM. *Nanotechnology* **2010**, *21*, 025701.

(139) Challa, S. R.; Delariva, A. T.; Hansen, T. W.; Helveg, S.; Sehested, J.; Hansen, P. L.; Garzon, F.; Datye, A. K. Relating Rates of Catalyst Sintering to the Disappearance of Individual Nanoparticles during Ostwald Ripening. *J. Am. Chem. Soc.* **2011**, *133*, 20672–20675.

(140) Chang, S. L. Y.; Barnard, A. S.; Dwyer, C.; Hansen, T. W.; Wagner, J. B.; Dunin-Borkowski, R. E.; Weyland, M.; Konishi, H.; Xu, H. Stability of Porous Platinum Nanoparticles: Combined In Situ TEM and Theoretical Study. *J. Phys. Chem. Lett.* **2012**, *3*, 1106–1110.

(141) Chen, H.; Yu, Y.; Xin, H. L.; Newton, K. A.; Holtz, M. E.; Wang, D.; Muller, D. A.; Abrun, D.; Disalvo, F. J.; Abruña, H. D. Coalescence in the Thermal Annealing of Nanoparticles: An in Situ STEM Study of the Growth Mechanisms of Ordered Pt–Fe Nanoparticles in a KCl Matrix. *Chem. Mater.* **2013**, *25*, 1436–1442.

(142) Yoshida, K.; Xudong, Z.; Bright, A. N.; Saitoh, K.; Tanaka, N. Dynamic Environmental Transmission Electron Microscopy Observation of Platinum Electrode Catalyst Deactivation in a Proton-Exchange-Membrane Fuel Cell. *Nanotechnology* **2013**, *24*, 065705.

(143) Behafarid, F.; Pandey, S.; Diaz, R. E.; Stach, E. A.; Roldán Cuenya, B. An in Situ Transmission Electron Microscopy Study of Sintering and Redispersion Phenomena over Size-Selected Metal Nanoparticles: Environmental Effects. *Phys. Chem. Chem. Phys.* **2014**, *16*, 18176.

(144) Martin, T. E.; Gai, P. L.; Boyes, E. D. Dynamic Imaging of Ostwald Ripening by Environmental Scanning Transmission Electron Microscopy. *ChemCatChem* **2015**, *7*, 3705–3711.

(145) Wu, F.; Yao, N. Advances in Windowed Gas Cells for in-Situ TEM Studies. *Nano Energy* **2015**, *13*, 1–22.

- (146) Creemer, J. F.; Helveg, S.; Hoveling, G. H.; Ullmann, S.; Molenbroek, A. M.; Sarro, P. M.; Zandbergen, H. W. Atomic-Scale Electron Microscopy at Ambient Pressure. *Ultramicroscopy* **2008**, *108*, 993–998.
- (147) Creemer, J. F.; Helveg, S.; Kooyman, P. J.; Molenbroek, A. M.; Zandbergen, H. W.; Sarro, P. M. A MEMS Reactor for Atomic-Scale Microscopy of Nanomaterials Under Industrially Relevant Conditions. *J. Microelectromechanical Syst.* **2010**, *19*, 254–264.
- (148) Jonge, N. De; Bigelow, W. C.; Veith, G. M. Atmospheric Pressure Scanning Transmission Electron Microscopy. **2010**, 1028–1031.
- (149) Yaguchi, T.; Suzuki, M.; Watabe, A.; Nagakubo, Y.; Ueda, K.; Kamino, T. Development of a High Temperature-Atmospheric Pressure Environmental Cell for High-Resolution TEM. *J. Electron Microsc.* **2011**, *60*, 217–225.
- (150) Allard, L. F.; Overbury, S. H.; Bigelow, W. C.; Katz, M. B.; Nackashi, D. P.; Damiano, Novel MEMS-Based Gas-Cell/Heating Specimen Holder Provides Advanced Imaging Capabilities for In Situ Reaction Studies. *Microsc. Microanal.* **2012**, *18*, 656–666.
- (151) Chen, Y.; Palmer, R. E.; Wilcoxon, J. P. Sintering of Passivated Gold Nanoparticles under the Electron Beam. *Langmuir* **2006**, *22*, 2851–2855.
- (152) Wang, R.; Zhang, H.; Farle, M.; Kisielowski, C. Structural Stability of Icosahedral FePt Nanoparticles. *Nanoscale* **2009**, *1*, 276–279.
- (153) Alloyeau, D.; Oikawa, T.; Nelayah, J.; Wang, G.; Ricolleau, C. Chemical Sensitivity Following Ostwald Ripening in Nanoalloys by High-Resolution Imaging with Single-Atom Chemical Sensitivity. *Appl. Phys. Lett.* **2012**, *101*, 121920.
- (154) Yuk, J. M.; Jeong, M.; Kim, S. Y.; Seo, H. K.; Kim, J.; Lee, J. Y. In Situ Atomic Imaging of Coalescence of Au Nanoparticles on Graphene: Rotation and Grain Boundary Migration. *Chem. Commun.* **2013**, *49*, 11479–11481.
- (155) Spenadel, L.; Boudart, M. Dispersion of Platinum on Supported Catalysts. *J. Phys. Chem.* **1960**, *64*, 204–207.
- (156) Wanke, S. Models for the Sintering of Supported Metal Catalysts. In *Progress in Catalyst Deactivation SE - 16*; Figueiredo, J., Ed.; NATO Advanced Study Institutes Series; Springer Netherlands, **1982**, *54*, 341–352.
- (157) Borchert, H.; Shevchenko, E. V; Robert, A.; Mekis, I.; Kornowski, A.; Grübel, G.; Weller, H. Determination of Nanocrystal Sizes: A Comparison of TEM, SAXS, and XRD Studies of Highly Monodisperse CoPt₃ Particles. *Langmuir* **2005**, *21*, 1931–1936.

- (158) Jentys, A. Estimation of Mean Size and Shape of Small Metal Particles by EXAFS. *Phys. Chem. Chem. Phys.* **1999**, *1*, 4059–4063.
- (159) Rehr, J. J.; Kas, J. J.; Vila, F. D.; Prange, M. P.; Jorissen, K. EXAFS as a Tool to Interrogate the Size and Shape of Mono and Bimetallic Catalyst Nanoparticles. *Phys. Chem. Chem. Phys.* **2010**, *12*, 5503–5513.
- (160) Paredis, K.; Ono, L. K.; Behafarid, F.; Zhang, Z.; Yang, J. C.; Frenkel, A. I.; Roldán Cuenya, B. Evolution of the Structure and Chemical State of Pd Nanoparticles during the in Situ Catalytic Reduction of NO with H₂. *J. Am. Chem. Soc.* **2011**, *133*, 13455–13464.
- (161) Paredis, K.; Ono, L. K.; Mostafa, S.; Li, L.; Zhang, Z.; Yang, J. C.; Barrio, L.; Frenkel, A. I.; Roldán Cuenya, B. Structure, Chemical Composition, and Reactivity Correlations during the in Situ Oxidation of 2-Propanol. *J. Am. Chem. Soc.* **2011**, *133*, 6728–6735.
- (162) Rieker, T.; Hanprasopwattana, A.; Datye, A. Particle Size Distribution Inferred from Small-Angle X-Ray. *Langmuir* **1999**, *15*, 638–641.
- (163) Smith, M. C.; Gilbert, J. A.; Mawdsley, J. R.; Seifert, S.; Myers, D. J. In Situ Small-Angle X-Ray Scattering Observation of Pt Catalyst Particle Growth during Potential Cycling. *J. Am. Chem. Soc.* **2008**, *130*, 8112–8113.
- (164) Ingham, B.; Lim, T. H.; Dotzler, C. J.; Henning, A.; Toney, M. F.; Tilley, R. D. How Nanoparticles Coalesce: An in Situ Study of Au Nanoparticle Aggregation and Grain Growth. *Chem. Mater.* **2011**, *23*, 3312–3317.
- (165) Russell, A. E. Size and Composition Distribution Dynamics of Alloy Nanoparticle Electrocatalysts Probed by Anomalous Small Angle X-Ray Scattering (ASAXS). *Faraday Discuss.* **2009**, *140*, 9.
- (166) Bowker, M. Resolving Catalytic Phenomena with Scanning Tunnelling Microscopy. *Phys. Chem. Chem. Phys.* **2007**, *9*, 3514–3521.
- (167) Yang, F.; Goodman, D. W. In Situ STM Studies of Model Catalysts. In *Scanning Tunneling Microscopy in Surface Science*; Wiley-VCH Verlag GmbH & Co. KGaA, **2009**; pp. 55–95.
- (168) Yang, F.; Chen, M. S.; Goodman, D. W. Sintering of Au Particles Supported on TiO₂ (110) during CO Oxidation. *J. Phys. Chem. C* **2009**, *113*, 254–260.
- (169) Ono, L. K.; Yuan, B.; Heinrich, H.; Roldán Cuenya, B. Formation and Thermal Stability of Platinum Oxides on Size-Selected Platinum Nanoparticles : Support Effects. *J. Phys. Chem. C* **2010**, *114*, 22119–22133.

- (170) Barth, C.; Foster, A. S.; Henry, C. R.; Shluger, A. L. Recent Trends in Surface Characterization and Chemistry with High-Resolution Scanning Force Methods. *Adv. Mater.* **2011**, *23*, 477–501.
- (171) Langhammer, C.; Larsson, E. M. Nanoplasmonic In Situ Spectroscopy for Catalysis Applications. *ACS Catal.* **2012**, *2*, 2036–2045.
- (172) Fredriksson, H.; Alaverdyan, Y.; Dmitriev, A.; Langhammer, C.; Sutherland, D. S.; Zäch, M.; Kasemo, B. Hole–Mask Colloidal Lithography. *Adv. Mater.* **2007**, *19*, 4297–4302.
- (173) Syrenova, S.; Wadell, C.; Langhammer, C. Shrinking-Hole Colloidal Lithography: Self-Aligned Nanofabrication of Complex Plasmonic Nanoantennas. *Nano Lett.* **2014**, *14*, 2655–2663.
- (174) Brunauer, S.; Emmett, P. H.; Teller, E. Adsorption of Gases in Multimolecular Layers. *J. Am. Chem. Soc.* **1938**, *60*, 309–319.
- (175) Tsukada, T.; Segawa, H.; Yasumori, A.; Okada, K. Crystallinity of Boehmite and Its Effect on the Phase Transition Temperature of Alumina. *J. Mater. Chem.* **1999**, *9*, 549–553.
- (176) Krokidis, X.; Raybaud, P.; Gobichon, A. E.; Rebours, B.; Euzen, P.; Toulhoat, H. Theoretical Study of the Dehydration Process of Boehmite to γ -Alumina. *J. Phys. Chem. B* **2001**, *105*, 5121–5130.
- (177) Paglia, G.; Buckley, C. E.; Udovic, T. J.; Rohl, A. L.; Jones, F.; Maitland, C. F.; Connolly, J. Boehmite-Derived γ -Alumina System. 2. Consideration of Hydrogen and Surface Effects. *Chem. Mater.* **2004**, *16*, 1914–1923.
- (178a) Evaldsson, L.; Löwendahl, L.; Otterstedt, J.-E. Fibrillar Alumina as a Wash-Coat on Monoliths in the Catalytic Oxidation of Xylene. *Appl. Catal.* **1989**, *55*, 123–136.
- (178b) Löwendahl, L.; Otterstedt, J.-E. Effect of Hydrothermal Treatment on Alumina as Support for Noble Metal Catalysts. *Appl. Catal.* **1990**, *59*, 89–102.
- (179) Paglia, G.; Buckley, C. E.; Rohl, A. L.; Hart, R. D.; Winter, K.; Studer, A. J.; Hunter, B. A.; Hanna, J. V. Boehmite Derived γ -Alumina System. 1. Structural Evolution with Temperature, with the Identification and Structural Determination of a New Transition Phase, γ' -Alumina. *Chem. Mater.* **2004**, *16*, 220–236.
- (180) Munnik, P.; de Jongh, P. E.; de Jong, K. P. Recent Developments in the Synthesis of Supported Catalysts. *Chem. Rev.* **2015**, *115*, 6687–6718.
- (181) Grant, A. W.; Hu, Q.; Kasemo, B. Transmission Electron Microscopy “Windows” for Nanofabricated Structures. *Nanotechnology* **2004**, *15*, 1175–1181.

- (182) Faraday, M. The Bakerian Lecture: Experimental Relations of Gold (and Other Metals) to Light. *Philos. Trans. R. Soc. London* **1857**, *147*, 145–181.
- (183) Dahmen, C.; von Plessen, G. Optical Effects of Metallic Nanoparticles. *Australian Journal of Chemistry*, **2007**, *60*, 447–456.
- (184) Ringe, E.; Sharma, B.; Henry, A.-I.; Marks, L. D.; Van Duyne, R. P. Single Nanoparticle Plasmonics. *Phys. Chem. Chem. Phys.* **2013**, *15*, 4110–4129.
- (185) Mayer, K. M.; Hafner, J. H. Localized Surface Plasmon Resonance Sensors. *Chem. Rev.* **2011**, *111*, 3828–3857.
- (186) Zhao, J.; Pinchuk, A. O.; McMahan, J. M.; Li, S.; Ausman, L. K.; Atkinson, A. L.; Schatz, G. C. Methods for Describing the Electromagnetic Properties of Silver and Gold Nanoparticles. *Acc. Chem. Res.* **2008**, *41*, 1710–1720.
- (187) Dahlin, A. B.; Tegenfeldt, J. O.; Höök, F. Improving the Instrumental Resolution of Sensors Based on Localized Surface Plasmon Resonance. *Anal. Chem.* **2006**, *78*, 4416–4423.
- (188) Anker, J. N.; Hall, W. P.; Lyandres, O.; Shah, N. C.; Zhao, J.; Van Duyne, R. P. Biosensing with Plasmonic Nanosensors. *Nat. Mater.* **2008**, *7*, 442–453.
- (189) Larsson, E. M.; Langhammer, C.; Zorić, I.; Kasemo, B. Nanoplasmonic Probes of Catalytic Reactions. *Science* **2009**, *326*, 1091–1094.
- (190) Langhammer, C.; Larsson, E. M.; Kasemo, B.; Zorić, I. Indirect Nanoplasmonic Sensing: Ultrasensitive Experimental Platform for Nanomaterials Science and Optical Nanocalorimetry. *Nano Lett.* **2010**, *10*, 3529–3538.
- (191) Larsson, E. M.; Syrenova, S.; Langhammer, C. Nanoplasmonic Sensing for Nanomaterials Science. *Nanophotonics* **2012**, *1*, 249–266.
- (192) Jing, C.; Rawson, F. J.; Zhou, H.; Shi, X.; Li, W. H.; Li, D. W.; Long, Y. T. New Insights into Electrocatalysis Based on Plasmon Resonance for the Real-Time Monitoring of Catalytic Events on Single Gold Nanorods. *Anal. Chem.* **2014**, *86*, 5513–5518.
- (193) Li, K.; Wang, K.; Qin, W.; Deng, S.; Li, D.; Shi, J.; Huang, Q.; Pan, C. DNA-Directed Assembly of Gold Nanohalo for Quantitative Plasmonic Imaging of Single-Particle Catalysis. *J. Am. Chem. Soc.* **2015**, *137*, 4292–4295.
- (194) Olson, J.; Dominguez-Medina, S.; Hoggard, A.; Wang, L.-Y.; Chang, W.-S.; Link, S. Optical Characterization of Single Plasmonic Nanoparticles. *Chem. Soc. Rev.* **2015**, *44*, 40–57.

- (195) Syrenova, S.; Wadell, C.; Nugroho, F. A. A.; Gschneidner, T. A.; Diaz Fernandez, Y. A.; Nalin, G.; Świtlik, D.; Westerlund, F.; Antosiewicz, T. J.; Zhdanov, V. P.; Moth-Poulsen, K.; Langhammer, C. Hydride Formation Thermodynamics and Hysteresis in Individual Pd Nanocrystals with Different Size and Shape. *Nat. Mater.* **2015**, *14*, 1–10.
- (196) Antosiewicz, T. J.; Wadell, C.; Langhammer, C.; Antosiewicz, T. J.; Wadell, C.; Langhammer, C. Plasmon-Assisted Indirect Light Absorption Engineering in Small Transition Metal Catalyst Nanoparticles. *Adv. Optical Mat.* **2015**, *3*, 1591–1599.
- (197) Larsson, E. M.; Millet, J.; Gustafsson, S.; Skoglundh, M.; Zhdanov, V. P.; Langhammer, C. Real Time Indirect Nanoplasmonic in Situ Spectroscopy of Catalyst Nanoparticle Sintering. *ACS Catal.* **2012**, *2*, 238–245.
- (198) Williams, D. B.; Carter, C. B. *Transmission Electron Microscopy-A Textbook for Materials Science*; 2nd, Ed.; Springer, **2009**.
- (199) Herzinger, C. M.; Johs, B.; McGahan, W. A.; Woollam, J. A.; Paulson, W. Ellipsometric Determination of Optical Constants for Silicon and Thermally Grown Silicon Dioxide via a Multi-Sample, Multi-Wavelength, Multi-Angle Investigation. *J. Appl. Phys.* **1998**, *83*, 3323.
- (200) Huang, F. H.; Li, C.-Y. Ripening of Platinum Particles on Aluminum Oxide. *Scr. Metall.* **1973**, *7*, 1239–1243.
- (201) Tabib Zadeh Adibi, P.; Mazzotta, F.; Antosiewicz, T. J.; Skoglundh, M.; Grönbeck, H.; Langhammer, C. In Situ Plasmonic Sensing of Platinum Model Catalyst Sintering on Different Oxide Supports and in O₂ and NO₂ Atmospheres with Different Concentrations. *ACS Catal.* **2015**, *5*, 426–432.